Phosphorylated Lamin A targets active enhancers and is associated with abnormal transcriptional activation in progeria

Kohta Ikegami[1,3]*, Stefano Secchia[3,4,†], Jason D. Lieb[3†], Ivan P. Moskowitz[1–3]

Departments of [1]Pediatrics, [2]Pathology, and [3]Human Genetics, The University of Chicago, Chicago, Illinois, USA

[4]Department of Biology, Lund University, Lund, Sweden

[†]Present address:

- Genome Biology Unit, European Molecular Biology Laboratory, Heidelberg, Germany (S.S.)
- Independent (J.D.L.)

*Correspondence: ikgmk@uchicago.edu (Kohta Ikegami)

20 **ABSTRACT**

LMNA encodes nuclear lamin A/C that tethers lamina-associated domains (LADs) to the nuclear lamina. Hutchinson-Gilford progeria is a premature aging disorder caused by heterozygous *LMNA* point mutations, however, the mechanism by which *LMNA* mutations cause progeria is unclear. We report that Ser22-phosphorylated LMNA (pS22-LMNA) was localized to the interior of the nucleus in human
25 fibroblasts throughout the cell cycle. pS22-LMNA interacted with a specific subset of putative active enhancers, not LADs, primarily at locations co-bound by the transcriptional activator c-Jun. In progeria-patient fibroblasts, some pS22-LMNA-binding sites were lost whereas new pS22-LMNA-binding sites emerged at abnormal locations. New pS22-LMNA-binding in progeria cells was accompanied by increased H3K27 acetylation, increased c-Jun binding, and upregulated expression of genes implicated
30 in coronary artery diseases, hypertension, and cardiomegaly, clinical components of progeria. Thus, pS22-LMNA bound to enhancers and progeria mutations affected pS22-LMNA-bound enhancer function. These observations expand the genomic role of LMNA to include direct enhancer binding and modulation, and introduce a novel molecular mechanism whereby LMNA mutation may contribute to disease distinct from LMNA's role at the nuclear lamina.

35

INTRODUCTION

Nuclear lamins polymerize to compose the nuclear lamina, a protein meshwork that underlies the nuclear membrane and provides structural support to the nucleus (Aebi et al., 1986; Gerace et al., 1978; Goldman et al., 1986). There are two major nuclear lamin types, A-type and B-type (Dittmer and Misteli, 2011). A-type lamins (Lamin A and Lamin C) are specific to vertebrates, expressed in differentiated cells, and encoded by *LMNA* in humans (Dittmer and Misteli, 2011). Point mutations in the *LMNA* gene cause a spectrum of human degenerative disorders including cardiomyopathies, muscular dystrophies, and the premature aging disorder Hutchinson-Gilford progeria (Worman et al., 2009). The molecular mechanisms underlying the disorders caused by *LMNA* mutations remain unclear.

Nuclear lamins including LMNA interact with large heterochromatin domains called lamina-associated domains (LADs) (Lund et al., 2014; Meuleman et al., 2012; van Steensel and Belmont, 2017). By interacting with LADs, nuclear lamins are implicated in spatial organization of chromosomal regions (van Steensel and Belmont, 2017). Genes in LADs are usually transcriptionally inactive (Guelen et al., 2008; Ikegami et al., 2010; Lund et al., 2014; Meuleman et al., 2012; Pickersgill et al., 2006). The relationship between nuclear lamin binding and transcriptional silencing of genes at the nuclear periphery, located in LADs, remains an area of active investigation. Tethering of genes to the nuclear periphery or inserting gene promoters into LADs does not always result in transcriptional repression (Finlan et al., 2008; Leemans et al., 2019; Reddy et al., 2008). Many gene promoters in LADs remain inactive when the activities are examined outside of LADs (Leemans et al., 2019). While one study reported that tethering of LMNA to gene promoters resulted in transcriptional downregulation (Lee et al., 2009), genetic depletion studies have shown that LMNA and other lamins are not required for repression of genes within LADs (Amendola and van Steensel, 2015; Kim et al., 2011; Zheng et al., 2018). Thus, whether nuclear lamins including LMNA have direct roles in transcriptional regulation has remained unclear.

LMNA has been observed in the interior of the nucleus, in addition to its localization at the nuclear lamina (Dechat et al., 2010a). Initial descriptions of nuclear-interior LMNA accompanied a model in which LMNA in the nuclear interior represented a long-sought “nuclear scaffold” protein (Barboro et al., 2002; Hozák et al., 1995). However, subsequent studies demonstrated that LMNA localized to the nuclear

interior was soluble and highly mobile (Broers et al., 1999; Shimi et al., 2008) thus present as a non-polymerized form and not constituting a scaffold structure. The specific function of LMNA in the nuclear interior has been difficult to ascertain, mainly due to a lack of understanding about how LMNA is directed to the nuclear interior, and a lack of laboratory approaches to isolate nuclear-interior LMNA.

Polymerization and depolymerization of nuclear lamins, required for nuclear envelope breakdown and the cell cycle, are regulated by phosphorylation of specific serine residues (Gerace and Blobel, 1980; Heald and McKeon, 1990; Peter et al., 1990; Ward and Kirschner, 1990). Ser22 (S22) and Ser392 (S392) of LMNA are well characterized and are known as “mitotic sites” because they are phosphorylated during mitosis, leading to LMNA depolymerization (Heald and McKeon, 1990; Peter et al., 1990; Ward and Kirschner, 1990). Early studies reported that phosphorylation of S22 and S392 begins at late G2 stage and is mediated by CDK1/Cyclin B, a kinase complex that promotes cell-cycle progression from G2 to mitosis (Georgatos et al., 1997; Heald and McKeon, 1990; Ward and Kirschner, 1990). More recently, S22 and S392 phosphorylation have been reported in the nuclear interior of interphase cells (Kochin et al., 2014), suggesting that S22/S392-phosphorylated, non-polymerized LMNA may represent a nuclear-interior pool of LMNA in interphase cells (Torvaldson et al., 2015). Separate studies proposed that S22 and S392 phosphorylation are increased upon changes in the mechanical environment of the cell and promote LMNA disassembly and degradation (Buxboim et al., 2014; Swift et al., 2013). Therefore, LMNA S22/S392 phosphorylation has been associated with mitotic nuclear lamina disassembly, but also with alternate cellular contexts in which its function remains unclear.

Hutchinson-Gilford progeria, caused by heterozygous *LMNA* mutations, is a rare, early-childhood, and fatal syndrome characterized by various symptoms including alopecia, joint contractures, loss of subcutaneous fat, sclerodermatous skin, and osteolysis (Gordon et al., 2003). Progeria patients invariably develop arteriosclerosis that ultimately causes death from myocardial infarction, heart failure, or stroke by the second decade of life (Merideth et al., 2008). The progeria mutations cause abnormal *LMNA* mRNA splicing, producing a mutant LMNA protein called “progerin” that lacks a part of the C-terminal tail domain (Eriksson et al., 2003). The C-terminal tail in wild-type LMNA harbors a protease cleavage site used for LMNA maturation and domains for protein, chromatin, and DNA interactions (Simon and Wilson,

90 2013). The C-terminal deletion in progerin results in permanent farnesylation that promotes nuclear membrane association of progerin (Goldman et al., 2004). In addition, the C-terminus in progerin exhibits reduced DNA and chromatin binding affinity *in vitro (Bruston et al., 2010)*. Because the functional unit of LMNA is a dimer, the progeria mutations have been postulated to function as dominant negative alleles, producing progerin that may disrupt the normal functions of wild-type LMNA (Gordon et al., 2014; Lee et
95 al., 2016). For example, LMNA's interactions with LADs are disrupted in progeria-patient fibroblasts (McCord et al., 2012). The effect of progeria mutations on the function of nuclear-interior LMNA has not been explored.

In this study, we report that S22-phosphorylated LMNA (pS22-LMNA) binds to genomic sites characteristic of active enhancers genome-wide in human fibroblasts. pS22-LMNA-binding sites
100 corresponded to a specific subset of accessible chromatin sites co-bound by the transcriptional activator c-Jun. In progeria-patient fibroblasts, a subset of pS22-LMNA-binding sites were lost while new pS22-LMNA-binding sites emerged at abnormal locations. Gains of pS22-LMNA-binding sites in progeria were accompanied by increased c-Jun binding, increased H3K27 acetylation, and up-regulation of nearby genes relevant to progeria pathogenesis. In contrast, LAD alterations could not explain most gene
105 expression alterations in progeria cell lines. We propose that LMNA in the nuclear interior positively modulates enhancer activity, separate from its role at LADs, and that LMNA's role at enhancers contributes to progeria pathogenesis.

RESULTS

110 **pS22-LMNA is localized in the interior of the nucleus throughout the cell cycle**

In this study, we interrogated S22-phosphorylated LMNA (pS22-LMNA) as a candidate functional non-polymerized LMNA in the nuclear interior because pS22-LMNA represents a depolymerized form of LMNA during mitosis (Gerace and Blobel, 1980; Heald and McKeon, 1990; Peter et al., 1990; Ward and Kirschner, 1990) (**Fig. 1A**). Prior studies have observed S22 phosphorylation also in interphase (Kochin
115 et al., 2014), but it has been attributed to a result of a mechanical stress (Buxboim et al., 2014; Swift et al., 2013). We therefore undertook experiments to determine the generality of pS22-LMNA localization in the nuclear interior in unperturbed normal human fibroblasts. We first confirmed the specificity of the anti-pS22-LMNA antibody (antigen: S22-phosphorylated N-terminal peptide) toward phosphorylation, and the specificity of the anti-non-phosphorylated-S22-LMNA antibody (non-pS22-LMNA; antigen: non-
120 phosphorylated aa2-29) toward the non-phosphorylated state by phosphatase treatment of protein blots followed by western blotting (**Fig. 1B**). Immunofluorescence microscopy of hTERT-immortalized human fibroblast BJ-5ta using these antibodies showed that pS22-LMNA signals were present in the nuclear interior, whereas non-pS22-LMNA signals were localized to the nuclear periphery (**Fig. 1C**). The pS22-LMNA and non-pS22-LMNA immunofluorescence signals were absent in a *LMNA*$^{-/-}$ fibroblast line derived
125 from BJ-5ta, confirming the specificity of the LMNA localization signals (**Fig. 1C; Fig. S1A**). At interphase stages, pS22-LMNA was detectable in the nuclear interior while non-pS22-LMNA was localized to the nuclear periphery (*Early G1* and *Interphase* in **Fig. 1D**). At late G2, pS22-LMNA signals increased dramatically, consistent with the model that S22 is phosphorylated during the G2-to-M transition for LMNA depolymerization (Peter et al., 1990) (*Late G2* in **Fig. 1D**). During mitosis, when the nuclear envelope is
130 absent, strong pS22-LMNA signal was observed throughout the cytoplasm whereas non-pS22-LMNA became undetectable, indicating that all LMNA molecules were S22-phosphorylated during mitosis (*Prophase* and *Metaphase* in **Fig. 1D**). Consistent with the cell-cycle dynamics of pS22-LMNA observed by microscopy, western blotting of cell-cycle synchronized BJ-5ta cells detected pS22-LMNA in G0 and G1/S phases, followed by an increase of the signal during G2/M phase (**Fig. E, F; Fig. S1B, S1C**). Flow
135 cytometry of unsynchronized BJ-5ta cells stained for pS22-LMNA and DNA further confirmed that pS22-

LMNA is present in G0/G1, S, and G2/M phases (**Fig. G, H; Fig. S1D)**. Thus, in normal unperturbed fibroblasts, LMNA exists at least in two forms throughout interphase: the non-S22-phosphorylated form at the nuclear lamina and the S22-phosphorylated form in the nuclear interior.

140 **pS22-LMNA interacts with genomic sites outside of lamina-associated domains**

Given LMNA's ability to interact with DNA and chromatin (Lund et al., 2014; Meuleman et al., 2012; Stierlé et al., 2003; Taniura et al., 1995), we hypothesized that pS22-LMNA interacts with the genome. To test this hypothesis, we performed ChIP-seq in asynchronous BJ-5ta cells for pS22-LMNA and for non-pS22-LMNA as a comparison. In sharp contrast to non-pS22-LMNA that interacted with megabase-wide
145 lamina-associated domains (LADs), pS22-LMNA exhibited point-source enrichment at discrete sites located outside of LADs (**Fig. 2A–C; Fig. S2A, B**). We identified 22,966 genomic sites bound by pS22-LMNA ("pLMNA-binding sites" thereafter) genome-wide. The pS22-LMNA ChIP-seq signals were abolished in the BJ-5ta-derived *LMNA*$^{-/-}$ cell line, confirming the specificity of the pS22-LMNA ChIP-seq signals in wild-type BJ-5ta (**Fig. 2A, B**). Consistent with the increased abundance of pS22-LMNA in G2/M
150 (**Fig. 1**), pS22-LMNA ChIP-seq signals were stronger in FACS-sorted G2/M-stage BJ-5ta cells than sorted G0/G1-stage cells (Mann-Whitney *U* test P $<2\times10^{-16}$; **Fig. S2C, D**). To examine the chromatin localization of pS22-LMNA with a different approach, we performed anti-Ty1 tag ChIP-seq on BJ-5ta cells overexpressing Ty1-tagged Lamin A, either with phospho-mimetic mutations (S22D/S392D), phospho-deficient mutations (S22A/S392A), or without mutations. Strikingly, phospho-mimetic Ty1-Lamin A was
155 strongly enriched at pLMNA-binding sites (**Fig. 2D; Fig. S2E**). Consistent with the hypothesis that pS22-LMNA is the predominant species that binds to pLMNA-binding sites, phospho-mimetic Ty1-Lamin A showed stronger ChIP signal than wild-type Ty1-Lamin A at pLMNA-binding sites (one-sample *t*-test on Log_2 difference between the mutant and wild type $P<2\times10^{-16}$), and phospho-deficient Ty1-Lamin A showed less ChIP signal than wild-type Ty1-Lamin A ($P<2\times10^{-16}$) (**Fig. 2D, E; Fig. S2E**). At LADs, in
160 contrast, phospho-deficient Ty1-Lamin A showed stronger ChIP signal than wild-type Ty1-Lamin A (one-sample *t*-test on Log_2 difference between the mutant and wild type $P<2\times10^{-16}$), while phospho-mimetic Ty1-Lamin A showed far weaker ChIP signal than wild-type Ty1-Lamin A ($P<2\times10^{-16}$) (**Fig. 2E**). Together,

these experiments revealed that S22/S392-phosphorylated LMNA has strong affinity to genomic sites outside of LADs.

165

pS22-LMNA physically associates with putative active enhancers

Analysis of the genomic features of pS22-LMNA-binding sites indicated that these sites exhibit characteristics of active enhancers. First, a vast majority of the 22,966 pLMNA-binding sites in BJ-5ta fibroblasts were located distal to the transcription start sites (TSSs) of genes (89% outside of –1000 kb
170 to +500 bp of TSSs) (**Fig. 2F**). Second, ATAC-seq in BJ-5ta showed that 88% of pLMNA-binding sites coincided with regions of accessible chromatin, a feature of regulatory regions (**Fig. 2B, F; Fig. S3A**). Third, H3K27ac ChIP-seq in BJ-5ta showed that 82% of pLMNA-binding sites coincided with regions enriched for H3K27ac, a histone modification associated with active enhancers and promoters (**Fig. 2B, F; Fig. S3A**). Fourth, H3K4me3 ChIP-seq in BJ-5ta found that only 13% of pLMNA-binding sites
175 coincided with regions enriched for H3K4me3, a histone modification associated with active promoters (**Fig. 2B, F; Fig. S3A**). Together, the strong association of pLMNA-binding sites with H3K27ac but not H3K4me3 suggested a binding preference of pS22-LMNA for enhancers over promoters. Fifth, comparison of the 22,966 pLMNA-binding sites with the chromatin state annotations in dermal fibroblasts (Roadmap Epigenomics Consortium et al., 2015) found that 59% of pLMNA-binding sites were located
180 in regions annotated as “Enhancers” (Permutation test $P<0.001$), whereas a smaller fraction of 16% were in “Active TSSs” ($P<0.001$) (**Fig. 2G**). Finally, although nearly all pLMNA-binding sites corresponded to accessible chromatin and H3K27ac-marked sites, pLMNA-binding sites corresponded to a minor subset of all accessible chromatin sites (26%) or all H3K27ac-marked sites (14%) in BJ-5ta (**Fig. S3A, B**). Thus, pS22-LMNA physically associates with a specific subset of distal, enhancer-like elements.

185

pLMNA-binding sites are strongly bound by the c-Jun transcription factor

Localization of pLMNA-binding sites at locations indicative of regulatory elements led us to inquire about specific transcription factors that may co-occupy pLMNA-binding sites with pS22-LMNA. We searched for DNA motifs over-represented at pLMNA-binding sites. We found that transcription factor binding

190 motifs for AP-1 (MEME E-value (Machanick and Bailey, 2011) $E=1x10^{-196}$), FOX ($E=6x10^{-127}$), and RUNX ($E=2x10^{-25}$) were overrepresented within pLMNA-binding sites (+/–75 bp of the pLMNA-binding-site center), relative to all accessible chromatin sites identified by ATAC-seq in BJ-5ta (**Fig. 3A**). Among those motifs, the AP-1 motif was present at the highest frequency at pLMNA-binding sites (9,250 pLMNA-binding sites, 41%), with a peak frequency located at the center of pLMNA-binding sites (**Fig. 3A**). To
195 test whether AP-1 transcription factors bind pLMNA-binding sites, we performed ChIP-seq in BJ-5ta for c-Jun, a core protein of the AP-1 dimeric transcription factors. Strikingly, c-Jun was strongly enriched at almost all pLMNA-binding sites (92% of 500-bp windows that contained pLMNA-binding sites; Fisher's exact test $P<2x10^{-16}$) (**Fig. 3B–D**). c-Jun binding at pLMNA-binding sites was much stronger than that outside of pLMNA-binding sites (Mann-Whitney *U* test, $P<2x10^{-16}$; **Fig. 3E**). pS22-LMNA ChIP signals
200 were strongly positively correlated with c-Jun ChIP signals (Pearson correlation coefficient r=0.63) at the 22,966 pLMNA-binding sites (**Fig. 3F**). Correlation with H3K27ac signals or ATAC-seq signals was much weaker (r=0.31 for K27ac, r=0.28 for ATAC) (**Fig. 3F**). The strong association between pS22-LMNA binding and c-Jun binding suggests that c-Jun may have function at pS22-LMNA-bound sites.

205 **Genes abnormally up-regulated in progeria-patient fibroblasts are relevant to progeria phenotypes**

In Hutchinson-Gilford progeria, the presence of the mutant LMNA protein is thought to alter the normal functions of wild-type LMNA (Lee et al., 2016). We therefore investigated the possibility that altered pS22-LMNA binding to enhancers contributed to gene expression changes in progeria. We performed
210 transcriptome analysis to identify genes dysregulated in fibroblast cell lines from progeria patients. We performed RNA-seq on primary dermal fibroblasts from two progeria patients (AG11498 and HGADFN167) and two normal individuals with similar ages (GM07492 and GM08398) (**Table S2; Fig. S4A–C**). In addition, we obtained public RNA-seq data sets for primary dermal fibroblasts from ten progeria patients (AG11513, HGADFN188, HGADFN127, HGADFN164, HGADFN169, HGADFN178,
215 HGADFN122, HGADFN143, HGADFN367, and HGADFN167) and ten normal individuals with similar ages (GM00969, GM05565, GM00498, GM05381, GM05400, GM05757, GM00409, GM00499,

GM00038, and GM08398) (Fleischer et al., 2018) (**Table S2; Fig. S4A**). The RNA-seq datasets of the progeria patients were clustered and separated from those of the normal individuals along the second principal component, indicating a common gene expression signature among progeria-patient fibroblasts
220 (**Fig. 4A; Fig. S4D**; the first principal component corresponded to the study origin of the samples). Comparison between the 14 progeria RNA-seq data sets (for 11 distinct cell lines) and the 12 normal RNA-seq data sets (for 10 distinct cell lines after removing 2 outlier datasets; **Fig. S4D**) identified 1,117 dysregulated genes, 615 up-regulated in the progeria cell lines ("progeria-up" genes) and 502 down-regulated in the progeria cell lines ("progeria-down" genes) (**Fig. 4B, C**). The progeria-up genes were
225 strongly over-represented for specific DisGeNET-curated disease ontology terms (Piñero et al., 2017) (17 terms with $P<0.001$) that were well-documented progeria phenotypes, such as "infraction, middle cerebral artery" (Hypergeometric test (Zhou et al., 2019) $P=7x10^{-6}$) (Silvera et al., 2013), "coronary artery disease" ($P=2x10^{-5}$) (Olive et al., 2010), "cardiomegaly" ($P=4x10^{-5}$) (Prakash et al., 2018), and "hypertensive disease" ($P=1x10^{-4}$) (Merideth et al., 2008), and that were closely related to progeria
230 phenotypes, such as "juvenile arthritis" ($P=1x10^{-5}$) (Gordon et al., 2007) and "Congenital hypoplasia of femur" ($P=1x10^{-4}$) (Gordon et al., 2007) (**Fig. 4D**). The progeria-down genes were associated with only three DisGeNet disease terms ($P<0.001$), including two terms that might be related to progeria phenotypes including "hip joint varus deformity" (Gordon et al., 2007) ($P=6x10^{-4}$) and "short stature, mild" ($P=9x10^{-4}$) (Gordon et al., 2011) (**Fig. 4D**). Thus, among genes dysregulated in progeria-patient fibroblast
235 lines, up-regulated genes were highly relevant to the clinical components of progeria.

LAD alterations do not explain most gene expression alterations in progeria

A prevailing model for the pathogenesis of progeria is that disruption of LADs causes loss of heterochromatin-associated histone modifications that in turn causes alteration of gene expression
240 (Gordon et al., 2014; McCord et al., 2012; Shumaker et al., 2006). To determine the extent to which LAD alterations in progeria could explain the gene expression changes in progeria, we performed ChIP-seq for non-pS22-LMNA in the progeria-patient fibroblast cell line AG11498 and the normal-individual fibroblast cell line GM07492 (**Fig. 5A**), which demonstrated transcriptomes representative of progeria

versus normal fibroblasts, respectively (**Fig. 4C**). We identified 2,735 union LADs, present in either the
245 progeria or the normal fibroblast or both. Of those, 353 LADs (13%) were present in the normal fibroblasts but absent in the progeria fibroblasts (called "lost LADs"), whereas 282 LADs (10%) were absent in the normal fibroblasts but present in the progeria fibroblasts (called "gained LADs") (**Fig. 5A–B; Fig. S5A**), confirming the previous observation that the LAD profile was altered in progeria (McCord et al., 2012). To determine if gained and lost LADs were associated with changes of the heterochromatin-associated
250 histone modifications H3K27me3 and H3K9me3, we performed ChIP-seq for H3K27me3 and H3K9me3 in the progeria cell line AG11498 and the normal cell line GM07492. H3K27me3 levels were reduced in the progeria cell line at both lost and gained LADs compared with the union LADs (Mann-Whitney *U* test $P=1x10^{-5}$ for lost LADs and $P=5x10^{-7}$ for gained LADs) (**Fig. 5C**), consistent with the previous report that H3K27me3 levels are globally reduced at gene-poor regions in progeria-patient fibroblasts (McCord et
255 al., 2012). H3K9me3 levels were reduced in progeria at lost LADs ($P=3x10^{-12}$), but increased at gained LADs ($P=3x10^{-12}$) (**Fig. 5D**), showing a positive correlation with the direction of LAD changes. Thus, we confirmed the prevailing model that LAD alterations in progeria are associated with changes of heterochromatin-associated histone modifications.

To determine the extent to which LAD changes were associated with gene expression changes,
260 we examined genes whose gene body or upstream 100-kb region intersected with lost or gained LADs. We asked if genes upregulated in progeria were affiliated with lost LADs or genes downregulated in progeria were affiliated with gained LADs. Only 23 out of 615 genes up-regulated in progeria intersected with lost LADs. Although this subset was a significant overrepresentation among progeria-up genes (Fisher's exact test $P=3x10^{-9}$), it accounted for only 3.7% of progeria-up genes (**Fig. 5E**). Similarly, only
265 11 out of 502 genes downregulated in progeria intersected with gained LADs. This subset, although over-represented among progeria-down genes ($P=8x10^{-4}$), accounted for only 2.2% of progeria-down genes. These data revealed that local LAD alterations could not explain the vast majority of gene expression changes in progeria, either upregulation of gene expression by LAD losses or downregulation of gene expression by LAD gains.

270

New pS22-LMNA-binding sites emerge in inappropriate locations in progeria-patient fibroblasts

We hypothesized that alterations of pS22-LMNA-binding sites in progeria might be associated with gene expression changes in progeria. To test this hypothesis, we performed pS22-LMNA ChIP-seq in the progeria-patient fibroblast cell line AG11498 and the normal-individual fibroblast cell line GM07492 (the
275 same cell lines used in non-pS22-LMNA ChIP-seq). We found a dramatic alteration of the pLMNA-binding site profile in the progeria fibroblasts: of 15,323 union pLMNA-binding sites identified in either of the two fibroblast lines or both, 2,796 pLMNA-binding sites (18%) were specific to the progeria fibroblast line (termed "gained pLMNA-binding sites") whereas 2,425 pLMNA-binding sites (16%) were specific to the normal fibroblast line (termed "lost" pLMNA-binding sites) (**Fig. 6A, B; Fig. S6A**). Gained pLMNA-binding
280 sites were highly over-represented within the "quiescent" chromatin-state annotation derived from normal dermal fibroblasts (Roadmap Epigenomics Consortium et al., 2015) (25% of gained pLMNA-binding sites vs. 10% of all pLMNA-binding sites; Fisher's exact test $P=2x10^{-144}$), whereas lost pLMNA-binding sites were over-represented in "enhancer" regions (72% of lost vs. 62% of all pLMNA-binding sites; $P=8x10^{-30}$) (**Fig. 6C**), suggesting that new pLMNA-binding sites emerged in inappropriate locations in progeria
285 that were quiescent in normal fibroblasts, while a subset of the wild-type enhancer pLMNA-binding sites were lost in progeria.

We hypothesized that changes in pLMNA-binding sites between progeria and normal fibroblasts reflected changes in the activity of specific enhancers. Because the level of pS22-LMNA binding was positively correlated with c-Jun and H3K27ac levels (**Fig. 3**), we hypothesized that gains of pLMNA-
290 binding sites in progeria may accompany gains in c-Jun and H3K27ac levels, whereas losses of pLMNA-binding sites may accompany losses of c-Jun and H3K27ac levels. To test this hypothesis, we performed c-Jun and H3K27ac ChIP-seq in the progeria cell line AG11498 and normal cell line GM07492. At the 2,796 gained pLMNA-binding sites, c-Jun and H3K27ac levels were strongly elevated in the progeria cell line compared with the normal cell line (**Fig. 6D, E; Fig. S6B, C**; Mann-Whitney *U* test $P<2x10^{-16}$ for both
295 c-Jun and H3K27ac). At the 2,425 lost pLMNA-binding sites, c-Jun and H3K27ac levels were strongly diminished in the progeria cell line compared with the normal cell line (**Fig. 6D, E; Fig. S6B, C**; $P<2x10^{-16}$ for both c-Jun and H3K27ac). Thus, the alteration of pS22-LMNA binding profile in progeria fibroblasts

was accompanied by alterations of c-Jun binding and H3K27ac levels at the pLMNA-binding sites, suggesting a link between the alteration of the pS22-LMNA binding profile and transcriptional regulation in progeria fibroblasts.

Gains of pS22-LMNA binding in progeria accompany abnormal transcriptional activation of genes clinically important to progeria pathophysiology

We hypothesized that gains and losses of pLMNA-binding sites in progeria were associated with gains and losses of transcription in progeria. We linked pLMNA-binding sites to genes, associating pLMNA-binding sites that reside in the gene body or the 100-kb upstream region of candidate target genes. By this metric, 85% of the 15,323 union pLMNA-binding sites were linked to at least one gene, and 1,225 genes were linked only to gained pLMNA-binding sites (11% of all genes), 1,144 genes were linked only to lost pLMNA-binding sites (9.9% of all genes), and 311 genes were linked to both gained and lost pLMNA-binding sites (2.7% of all genes) (**Fig. S6D**). Genes linked only to gained pLMNA-binding sites were highly over-represented among genes up-regulated in progeria (142 genes, 23%, $P=3x10^{-20}$), but not among genes down-regulated in progeria (47 genes, 9.3%, P=0.4) (**Fig. 6F**). Genes linked only to lost pLMNA-binding sites were over-represented among genes down-regulated in progeria (75 genes, 15%, $P=2x10^{-4}$), but not among genes upregulated in progeria (69 genes, 11%, P=0.2) (**Fig. 6F**). Thus, gains of pS22 LMNA binding were associated with up-regulation of genes, and losses of pS22 LMNA binding were associated with down-regulation of genes, in progeria fibroblasts, respectively. Interestingly, genes linked to both gained and lost pLMNA-binding sites were over-represented among genes upregulated in progeria (50 genes, 8.1%, $P=1x10^{-12}$), but not among genes downregulated in progeria (12 genes, 2.3%, P=0.7) (**Fig. 6F**), suggesting a dominant association between gains of pLMNA-binding and up-regulation of genes in progeria.

We hypothesized that progeria-up genes linked to gained pLMNA-binding sites may be relevant to progeria phenotypes. The progeria-up genes linked to gained pLMNA-binding sites (192 genes) were highly over-represented for DisGeNet disease ontology terms relevant to progeria phenotypes such as carotid artery disease (Hypergeometric test (Zhou et al., 2019) P=0.007) (Gerhard-Herman et al., 2012),

325 juvenile arthritis ($P=1x10^{-5}$) (Gordon et al., 2007), cardiomegaly ($P=4x10^{-5}$) (Prakash et al., 2018), and hypertensive disease (P=0.0001) (Merideth et al., 2008) (**Fig. 6G**). None of these terms were overrepresented among the progeria-up genes not linked to a pLMNA-binding site (423 genes) (**Fig. 6G**). Thus, gained pLMNA-binding sites marked a subset of abnormally activated genes in progeria that are highly relevant to progeria phenotypes. We propose that misdirection of pS22-LMNA to inappropriate
330 genomic locations is a novel mechanism for the transcriptional up-regulation of pathogenesis-related gene pathways in progeria (**Fig. 6H**).

DISCUSSION

335 Nuclear lamins have been extensively studied in the context of the nuclear lamina (Dechat et al., 2010b; van Steensel and Belmont, 2017). In this paper, we investigated the genomic localization and function of Ser22-phosphorylated nuclear lamin A/C (pS22-LMNA) localized to the interior of the nucleus. In stark contrast to nuclear-peripheral LMNA, which associates with megabase-wide heterochromatin domains (Lund et al., 2014; Meuleman et al., 2012), pS22-LMNA associated with kilobase-wide sites characteristic
340 of active enhancers. The existence of LMNA in the nuclear interior has been documented for decades (Barboro et al., 2002; Bridger et al., 1993; Buxboim et al., 2014; Gesson et al., 2016; Goldman et al., 1992; Hozák et al., 1995; Kochin et al., 2014; Moir et al., 1994; Naetar et al., 2008; Shimi et al., 2008; Swift et al., 2013), yet the specific function of nuclear-interior LMNA had been elusive. This report demonstrates that pS22-LMNA-binding sites were affiliated with the signature of enhancers and were
345 frequently co-occupied by the AP-1 transcription factor c-Jun, a strong transcriptional activator. Furthermore, gains and losses of pS22-LMNA-binding sites in progeria-patient cells were accompanied by increased or decreased local H3K27ac and up- or down-regulation of nearby genes, respectively. These observations provide evidence that nuclear-interior pS22-LMNA functions as a positive modulator of enhancer activity.

350 Decades of work have established that nuclear lamins at the nuclear lamina are associated with transcriptionally-inactive regions (Guelen et al., 2008; Ikegami et al., 2010; Meuleman et al., 2012; Pickersgill et al., 2006; van Steensel and Belmont, 2017). In this respect, the data showing that pS22-LMNA-binding sites exhibit the characteristics of active enhancers and are associated with active transcription is striking. The contrasting genomic localization patterns suggest that LMNA does not have
355 an intrinsic preference for LADs or pS22-LMNA-binding sites. Instead, our data suggest that the preference depends on the phosphorylation state of S22/S392, phosphorylation-driven subnuclear localization of LMNA, or both. Our finding that chromatin accessibility is not a strong predictor of the location of pS22-LMNA-binding sites suggests that distinct targeting mechanisms exist to direct pS22-LMNA to putative active enhancers. Given our observation that pS22-LMNA enrichment is strongly

360 correlated with c-Jun localization, c-Jun is a candidate for functioning to target pS22-LMNA to specific putative enhancers.

Recently, nuclear-interior LMNA has been studied in the context of its interaction with lamina-associated polypeptide 2 alpha (LAP2α) (Dechat et al., 2010a; Naetar et al., 2008). A study suggested that LAP2α-interacting LMNA associates with megabase-wide genomic regions that lie at euchromatin
365 regions without specific localization at promoters or enhancers (Gesson et al., 2016). pS22-LMNA binds to specific enhancer-like elements and promoters, and therefore, is likely distinct from LAP2α-interacting LMNA.

Altered gene expression programs have been reported in fibroblasts and other cell types derived from progeria patients (Csoka et al., 2004; Zhang et al., 2011), yet the underlying mechanisms have
370 remained unclear. A prevailing hypothesis suggests that progerin, the mutant LMNA protein expressed in progeria, accumulates at the nuclear lamina due to its permanent farnesylation and disrupts normal interactions between LMNA and LADs, causing heterochromatin disorganization and, in turn, alteration of expression of genes located in LADs (McCord et al., 2012; Shumaker et al., 2006). One limitation of this model is that it does not explain the specific and abundant gene expression changes that occur
375 outside of LADs. We propose an alternative hypothesis, in which mis-direction of pS22-LMNA to otherwise unbound enhancer regions or quiescent regions results in abnormal direct transcriptional activation of genes relevant to progeria pathogenesis. The molecular mechanisms for how pS22-LMNA is localized in altered locations in progeria-patient cells are an important area for future investigations.

pS22-LMNA has been regarded as a byproduct of mitotic nuclear envelope breakdown (Gerace
380 and Blobel, 1980) or disassembled lamins to be degraded when the nuclear lamina is compromised by mechanical stress (Buxboim et al., 2014; Swift et al., 2013). Our data that pS22-LMNA is present throughout interphase under unperturbed cellular conditions, localized at a specific subset of putative active enhancers, and associated with transcriptional alteration in progeria, suggests that pS22-LMNA is a previously-unrecognized functional species of LMNA in the interior of the nucleus. Much like the function
385 of nuclear lamins in transcriptional repression at the nuclear lamina remains to be under active investigation (Leemans et al., 2019), the causal relationship between pS22-LMNA binding at putative

enhancers and transcriptional regulation remains to be determined. Regardless, the characteristics of pS22-LMNA presented in this study offer a new foundation for investigating the function of LMNA and its relationship to human degenerative disorders caused by *LMNA* mutations.

390

ACKNOWLEDGEMENTS

We thank technical assistance from the University of Chicago Functional Genomics Core, the University of Chicago Cytometry and Antibody Technology Core, the University of Chicago Light Microscopy Core, and Princeton University Genomics Core Facility. This work was funded by NIH R21 AG054770-01A1 (K.I. and I.P.M.), NIH R01 HL126509 (I.P.M.), and the Progeria Research Foundation grant #2009-0028 (K.I. and J.D.L.).

AUTHOR CONTRIBUTIONS

K.I. and J.D.L conceived the study. K.I. and S.S. performed the experiments. K.I. analyzed the data and wrote the manuscript. J.D.L. and I.P.M. provided intellectual contributions and participated in manuscript writing.

DECLARATION OF INTERESTS

The authors declare no competing interests.

METHODS

Cell lines

BJ-5ta (ATCC catalog # CRL-4001) is a TERT-immortalized BJ skin fibroblast cell line that retains normal fibroblast cell growth phenotypes and does not exhibit transformed phenotypes (Jiang et al., 1999). Generation of the BJ-5ta-derived *LMNA*$^{-/-}$ cell line and BJ-5ta over-expressing wild-type and mutant *LMNA* transgenes is described in the following sections. Primary dermal fibroblasts used are GM07492 (source: thigh of 17-year-old male normal individual, Coriell Cell Repository), GM08398 (source: inguinal area of 8-year-old male normal individual, Coriell Cell Repository), AG11498 (source: thigh of 14-year-old male Hutchinson-Gilford progeria patient, Coriell Cell Repository), and HGADFN167 (source: posterior lower trunk of 8-year-old male Hutchinson-Gilford progeria patient, Progeria Research Foundation) (**Table S2**). We verified that, at the time of cell harvest, the progeria and control cells were not undergoing senescence (beta-galactosidase positive cells < 5%), a feature that late-passage progeria cells could manifest (Sieprath et al., 2015) (**Fig. S4B, C**).

Cell culture

All cells were cultured in standard cell-culture-treated plastic dishes (Nunc) unless otherwise noted. BJ-5ta and its derivatives were cultured in high-glucose DMEM (Gibco, 11965-092) containing 9% fetal bovine serum (FBS), 90 U/mL penicillin, 90 µg/mL streptomycin streptomycin at 37ºC under 5% CO_2. Primary skin fibroblasts were cultured in MEM Alpha (Gibco, 12561-056) containing 9% fetal bovine serum (FBS), 90 U/mL penicillin, 90 µg/mL streptomycin streptomycin at 37ºC under 5% CO_2.

Cell synchronization by thymidine block

BJ-5ta cells in the DMEM growth medium (above) were maintained at confluency for 2 days (G0 arrest by contact inhibition). The cells were then passaged to a culture plate at a low density in the DMEM growth medium supplemented with 2 mM thymidine (Sigma-Aldrich T9250) for 17 hours. This allowed cells to re-enter into the G1 stage of the cell cycle and then become arrested at the G1/S boundary. Cells were then washed and cultured with the growth medium with 2.5 µM deoxycytidine (without thymidine)

and harvested at 0, 4, 6, 8, 10, 12, and 14 hours later. As a reference, G0-arrested cells were released in the growth medium without thymidine and harvested 14 hours later ("asynchronous 14 hours").

440

Generation of LMNA$^{-/-}$ cell line

Briefly, wild-type BJ-5ta cells were transduced with two lentivirus vectors, each of which expressed *S. pyogenes* Cas9 and one of two short-guide RNAs (sgRNA1 and sgRNA3). sgRNA1 and sgRNA3 were designed to target the exon 1 of the *LMNA* gene. The transduced cells were clonally expanded. A clone

445 (clone ID cc1170-1AD2) that lacks Lamin A and Lamin C protein expression was obtained.

In detail, we first introduced DNA sequences for sgRNA1 (oligonucleotides KI223 and KI224; **Table S1**) or sgRNA3 (oligonucleotides KI227 and KI228; **Table S1**) into lentivirus vector LentiCRISPRv2 (a gift from Feng Zhang; Addgene plasmid # 52961) (Sanjana et al., 2014), yielding pKI9 (for sgRNA1) and pKI13 (for sgRNA3). HEK293FT cells were transfected with pKI9 or pKI13 together with packaging

450 vectors psPAX2 (a gift from Didier Trono; Addgene plasmid # 12260) and pCMV-VSV-G (a gift from Bob Weinberg; Addgene plasmid # 8454) (Stewart et al., 2003) to produce lentivirus. To transduce BJ-5ta cells with the lentivirus, BJ-5ta cell culture was mixed with cleared tissue-culture supernatant for sgRNA1 lentivirus and that for sgRNA3 (each at 0.25 dilution) in the presence of 7.5 μg/mL polybrene. Successfully transduced cells were selected by 3 μg/mL puromycin and seeded to 10-cm dishes with a

455 density of 100 cells per dish. Clonal populations were expanded and analyzed by western blotting for Lamin A and Lamin C protein expression. Clone cc1170-1AD2 lacked Lamin A and Lamin C protein expression and was used in this study.

Overexpression of Lamin A/C and Lamin A-mutants

460 Briefly, for stable expression of *LMNA* transgenes, lentivirus vectors containing cDNA for 3xTy1-tagged Lamin A or Lamin C or Lamin A phosphorylation-site mutants were transduced to wild-type BJ-5ta cells, and transduced cell populations were selected by puromycin. These transgenes were under the control of the EF1 alpha promoter.

In detail, we first cloned cDNAs for 3xTy1-tagged Lamin A, Lamin C, and Lamin A
465 phosphorylation-site mutants into lentivirus vector pCDH-EF1α-MCS-PGK-GFP-T2A-Puro (CD813A-1, System Biosciences). cDNA sequences for Lamin A, Lamin C, and phospho mutants were cloned from cDNA expression plasmids described previously (Kochin et al., 2014) (gifts from Drs. Robert Goldman and John E Eriksson). The 3xTy1 tag was incorporated using PCR (oligonucleotides KI253, KI243, and KI244; **Table S1**). Lentivectors for Ty1-Lamin A (pKI36), Ty1-Lamin C (pKI28), Ty1-Lamin A-S22A/S392A
470 (pKI111), and Ty1-Lamin A-S22D/S392D (pKI114) were transfected to HEK293FT cells to produce lentiviruses. Cleared tissue culture supernatant for Ty1-Lamin A and Ty1-Lamin C viruses were used in 1/2 dilution, and that for Ty1-Lamin A-S22A/S392A and Ty1-Lamin A-S22D/S392D viruses were used in 1/64 dilution to transduce wild-type BJ-5ta cells in the presence of 7.5 μg/mL polybrene. Transduced cell populations were selected under 3 μg/mL puromycin. The cell population IDs are cc1194-4-1 (Ty1-Lamin
475 A OE); cc1194-5-1 (Ty1-Lamin C OE); cc1255-2-6 (Ty1-Lamin A-S22A/S392A OE); and cc1255-3-6 (Ty1-Lamin A-S22D/S392D).

Western blot

Ten micrograms of total proteins were separated by SDS-PAGE and transferred to a PVDF membrane.
480 For phosphatase treatment, PVDF membranes were incubated with Lambda Protein Phosphatase (Lambda PP, 8 unit/μL final concentration, New England Biolabs P0753) in 1X NEBuffer for Protein MetalloPhosphatases supplemented with 1 mM MnCl2, 1% BSA, and 1% Triton at 30ºC for 2 hours. The control membranes were incubated in the buffer without Lambda PP. LMNA proteins were detected by rabbit monoclonal anti-phospho-Ser22-LMNA antibody D2B2E (Cell Signaling 13448S, Lot # 1) or mouse
485 monoclonal anti-non-phospho-Ser22-LMNA antibody E1 (Santa Cruz Biotechnology sc-376248, Lot # H2812) for **Fig. 1B, E**, and **Fig. 1SC**, or by rabbit polyclonal anti-LMNA antibody H-110 (Santa Cruz Biotechnology sc-20681, Lot # D1415) for **Fig. S1A**. The gel after protein transfer was counter-stained by coomassie to evaluate the loaded protein amount.

490 ***Flow cytometry***

For cell-cycle analysis by DAPI, detached cells were incubated with 70% cold ethanol at -20ºC for 12 hours or more for fixation. The fixed cells were incubated with FACS buffer (2% FBS, 1 mM EDTA, and 0.1% Tween 20 in PBS) for 10 min at RT. Cells were then incubated with PBS supplemented with 0.1% Triton and 1 µg/mL DAPI for 10 min at RT. The DAPI-stained cells were resuspended in FACS buffer and
495 then analyzed by Fortessa 4-15 HTS or Fortessa X20 5-18 flow cytometry analyzers (BD Biosciences).

To stain cells for pS22-LMNA, cells were fixed in PHEM buffer (60 mM PIPES-KOH pH7.5, 25 mM HEPES-KOH pH7.5, 10 mM EGTA, 4 mM $MgSO_4$) supplemented with 4% formaldehyde, 0.5% Triton, and 100 nM phosphatase inhibitor Nodularin (Enzo ALX-350-061) for 15 min at 37ºC. Cells were washed with FACS buffer supplemented with 5% normal goat serum and then incubated with FACS
500 buffer (see above) supplemented with Alexa-647-conjugated rabbit monoclonal anti-phospho-Ser22-LMNA antibody D2B2E (Cell Signaling 97262BC, Lot 1, 1:30 dilution) for 1 hour at 37ºC. Cells were counter-stained with 1 µg/mL DAPI in FACS buffer. The stained cells were analyzed by Fortessa 4-15 HTS or Fortessa X20 5-18 flow cytometry analyzers.

505 ***Immunofluorescence***

Cells were grown on uncoated coverslips under the standard culture condition (see *Cell Culture*). Cells were fixed in PHEM buffer (60 mM PIPES-KOH pH7.5, 25 mM HEPES-KOH pH7.5, 10 mM EGTA, 4 mM $MgSO_4$) supplemented with 4% formaldehyde, 0.5% Triton, and 100 nM phosphatase inhibitor Nodularin (Enzo ALX-350-061) for 10 min at 37ºC. Cells on coverslips were first blocked by 1% skim milk and 5%
510 goat serum in PBS, and then incubated with primary antibodies in blocking buffer. Antibodies used in immunofluorescence are: Alexa 647-conjugated rabbit monoclonal anti-phospho-Ser22-LMNA antibody D2B2E (Cell Signaling 97262BC, Lot 1, 1:100 dilution) and mouse monoclonal anti-non-phospho-Ser22-LMNA antibody E1 (Santa Cruz Biotechnology sc-376248, Lot # H2812, 1:5000). Cells were incubated with secondary antibodies, counterstained by DAPI, and cured in ProLong Gold mounting medium
515 (Molecular Probes, P36930). Cells were imaged using Leica SP8 confocal microscope with a 63x objective.

Senescence-associated beta-galactosidase assay

Cells were grown on coverslips and washed twice in PBS and fixed for 5 min in 2% formaldehyde and
520 0.2% glutaraldehyde in PBS. Cells were washed with PBS and incubated in X-gal staining solution (40 mM citric acid/sodium phosphate buffer, 5 mM $K_4[Fe(CN)_6]$ $3H_2O$, 5 mM $K_3[Fe(CN)_6]$, 150 mM NaCl, 2 mM $MgCl_2$, and 1 mg/mL X-gal) for 16 h at 37ºC. The coverslips were washed with PBS and mounted for microscopy. To determine the staining percentages, cells from 10 randomly selected areas at 20x magnification were counted.

525

ChIP-seq

Cells in culture dishes were crosslinked in 1% formaldehyde for 15 min, and the reaction was quenched by 125 mM glycine. Cross-linked cells were washed with LB1 (50 mM HEPES-KOH pH7.5, 140 mM NaCl, 1 mM EDTA, 10% glycerol, 0.5% NP40, 0.25% Triton X-100) and then with LB2 (200 mM NaCl, 1 mM
530 EDTA, 0.5 mM EGTA, and 10 mM Tris-HCl pH 8.0). For cell-cycle-stage specific ChIP, cross-linked cells were stained by DAPI (5 µg/mL) in LB1 for 5 min at RT, sorted based on the cellular DNA content using BD FACS Aria II or BD FACS Aria IIIu, and then washed with LB2. Cells were resuspended in LB3-Triton (1 mM EDTA, 0.5 mM EGTA, 10 mM Tris-HCl pH 8, 100 mM NaCl, 0.1% Na-Deoxycholate, 0.5% N-lauroyl sarcosine, 1% Triton), and chromatin was extracted by sonication. LB1, LB2, and LB3-Triton were
535 supplemented with 1x protease inhibitor cocktail (Calbiochem 539131) and 100 nM phosphatase inhibitor Nodularin (Enzo ALX-350-061). The cell extract was cleared by 14,000 g centrifugation for 10 min. An aliquot of cell extract was saved for input DNA sequencing.

For ChIP, cell extract from one million cells was incubated with antibodies in a 200-µL reaction for 12 hours or more. Antibodies used in ChIP are: rabbit monoclonal anti-phospho-Ser22-LMNA antibody
540 D2B2E (Cell Signaling 13448S, Lot No. 1; 5 µL per IP); mouse monoclonal anti-non-phospho-Ser22-LMNA antibody E1 (Santa Cruz Biotechnology sc-376248, Lot H2812; 10 µL per IP); mouse monoclonal anti-H3K27ac antibody (Wako MABI0309, Lot No. 14007; 2 µL per IP); mouse monoclonal anti-H3K4me3 antibody (Wako MABI14004, Lot No. 14004; 2 µL per IP); mouse monoclonal anti-Ty1 antibody

(Diagenode C15200054, Lot No. 005; 1 μL per IP); rabbit polyclonal anti-c-Jun antibody (Santa Cruz
545 Biotechnology sc-1694, Lot D1014; 20 μL per IP); rabbit polyclonal anti-H3K9me3 antibody (Abcam ab8898, Lot GR232099-3; 2 μL per IP); and rabbit polyclonal anti-H3K27me3 (Active Motif No. 39155, Lot No. 31814017; 2 μL per IP). Immunocomplex was captured by Protein A-conjugated sepharose beads (for rabbit antibodies) or Protein G-conjugated magnetic beads (for mouse antibodies) and washed. Immunoprecipitated DNA was reverse-crosslinked and used to construct high-throughput sequencing
550 libraries using NEBNext Ultra DNA Library Prep Kit (New England Biolabs, E7370). DNA libraries were processed on a Illumina HiSeq machine for single-end sequencing. Data processing steps are described in *ChIP-seq data processing*. ChIP-seq experiments are listed in **Table S3**.

ATAC-seq

555 One hundred thousand trypsinized cells were incubated with ATAC hypotonic buffer (10 mM Tris pH 7.5, 10 mM NaCl, 3 mM $MgCl_2$) at 4ºC for 10 min during 500 g centrifugation. Cells were incubated in Tagmentation mix (Tagmentation DNA buffer Illumina 15027866; Tagmentation DNA enzyme Illumina 15027865) at 37ºC for 30 min. Purified DNA was used to construct high-throughput sequencing libraries using NEBNext High-Fidelity 2x PCR Master Mix (New England Biolabs M0541). DNA libraries were
560 processed on a Illumina NextSeq machine for paired-end 41-nt sequencing. Data processing steps are described in *ATAC-seq data processing*. ATAC-seq experiments are listed in **Table S3**.

RNA-seq

Total RNAs were purified by Trizol LS (Invitrogen 10296028) and treated with DNase I (Invitrogen Turbo
565 DNase AM2238). mRNAs were isolated using NEBNext Poly(A) mRNA Magnetic Isolation Module (New England Biolabs E7490) and fragmented using Fragmentation Buffer (Ambion AM8740). cDNAs were synthesized using SuperScript II (Invitrogen 18064014), and non-directional high-throughput sequencing libraries were prepared using NEBNext Ultra DNA Library Prep Kit (New England Biolabs, E7370). Libraries were processed on the Illumina HiSeq platform for single-end 50-nt sequencing. Data

570 processing steps are described in *RNA-seq data processing*. RNA-seq experiments are listed in **Table S3**.

Blacklisted regions

Before performing data analyses, we excluded all genes and genomic features located in blacklisted
575 regions which are genomic regions that may cause misinterpretation due to high sequence redundancy, uncertain chromosomal locations, high signal background, haplotypes, or potential copy number variations (CNVs) between wild-type BJ-5ta and *LMNA*$^{-/-}$ BJ-5ta cells. The collection of such genomic regions were constructed from the following datasets (see *Public datasets*): assembly gaps in the hg19 reference genome, ENCODE-defined hg19 blacklisted regions, mitochondrion sequence (chrM),
580 haplotype chromosomes (chr*_*_hap*), unplaced contigs (chrUn_*), unlocalized contigs (chr*_*_random), and potential CNVs described below. To identify potential large CNVs between wild-type BJ-5ta and *LMNA*$^{-/-}$ BJ-5ta cells, input sequencing data for wild-type BJ-5ta (ID KI481) and *LMNA*$^{-/-}$ cells (ID KI489) were processed with CNV-seq (Xie and Tammi, 2009) with the following parameters: [–genome human –global-normalization –log2-threshold 0.5 –minimum-windows-required 3]. After
585 removing windows with low sequence coverage, candidate CNV windows that were overlapping or spaced within 500 kb were merged, and isolated windows smaller than 500 kb in size were removed. This yielded 5 candidate large CNVs (24 Mb in chr1; 15 Mb in chr 4; 2.7 Mb in chr19; 683 kb in chr2; and 528 kb in chrX). The blacklisted regions are listed in **Table S4**.

590 ***Gene annotation***

The Gencode V19 “Basic” gene annotation was downloaded from the UCSC genome browser. Of the total 99,901 transcripts in the list, we retained transcripts that met all of the following requirements: 1) “gene type” equals “transcript type”; 2) “transcript type” is either *protein_coding* or *antisense* or *lincRNA*; and 3) “transcript ID” appears only once in the list. This processing yielded 75,968 transcripts. To select
595 one transcribed unit per gene locus, the 75,968 transcripts were grouped by “gene symbol,” and within the group, transcripts were sorted by the “exon count” (largest first), then by “length” of transcribed region

(largest first), then by the alphanumeric order of the "transcript ID" (smallest first), and the transcript that appeared first in the group was chosen to represent the transcribed unit of that gene. In this processing, in general, a transcript with a largest number of annotated exons among other associated transcripts
600 represented the gene. After removing genes located within the blacklisted regions (see *Blacklisted regions*), we obtained 31,561 genes, which included 19,469 "protein_coding" genes.

ChIP-seq data processing

ChIP-seq experiments and sequencing depth are listed in **Table S3**. ChIP-seq reads were mapped to
605 the hg19 human reference genome using Bowtie2 with the default "--sensitive" parameter. Reads with MAPQ score greater than 20 were used in downstream analyses. Reads from biological replicates of ChIP and the corresponding input were processed by MACS2 (Zhang et al., 2008). In MACS2, duplicate reads were removed and a file for input-normalized per-base coverage of 200 nt-extended reads (fold enrichment score) was generated. In addition, for ChIP-seq with point-source enrichment profiles,
610 MACS2 was used to identify statistically overrepresented peak regions and peak summits using the following parameter set: [call peak -g hg --nomodel --extsize 200 --call-summits]. Peaks overlapping blacklisted regions (see *Blacklisted regions* section) were removed. We defined a summit as a unit of a protein binding site. MACS2 identified 22,966 pS22-LMNA-binding sites in BJ-5ta (**Table S5**); 79,799 H3K27ac-enriched sites in BJ-5ta (**Table S8**); 18,100 H3K4me3-enriched sites in BJ-5ta (**Table S9**);
615 87,988 c-Jun-enriched sites in BJ-5ta (**Table S10**).

ATAC-seq data processing

ATAC-seq experiments and sequencing depth are listed in **Table S3**. For alignment, the first 38 nt of the 41-nt reads in the 5′ to 3′ direction were used. The rationale of this trimming is that the minimum size of
620 DNA fragments that can be flanked by Tn5 transposition events has been estimated to be 38 bp (Picelli et al., 2014; Reznikoff, 2008), and therefore, a 41-nt read could contain a part of read-through adaptors. We aligned 38-nt reads to the hg19 reference genome using bowtie2 with following parameters: [-X 2000 --no-mixed --no-discordant --trim3 3]. The center of the active Tn5 dimer is estimated to be located +4-5

bases offset from the 5′-end of the transposition sites (Picelli et al., 2014; Reznikoff, 2008). To place the
625 Tn5 loading center at the center of aligned reads, the 5′-end of the plus-strand read was shifted 4 bp in the 5′-to-3′ direction and that of the minus-strand reads was shifted 5 bp in the 5′-to-3′ direction, and the shifted end (1 nt) was extended +/–100 bp. To generate background datasets that capture local bias of read coverage, the shifted read ends were extended +/–5,000 bp and used to construct local lambda background file. This local lambda file and the Tn5 density file were processed by MACS2's function
630 "bdgcomp" to generate the fold-enrichment file for Tn5 density and by MACS2's function "bdgpeakcall" to identify regions with statistically significant Tn5 enrichment (ATAC peaks). At P-value cutoff of $1x10^{-10}$, we obtained 73,933 ATAC peaks (**Table S7**).

RNA-seq data processing

635 RNA-seq experiments and sequencing depth are listed in **Table S3**. Public RNA-seq raw data files (fastq) for normal and progeria-patient fibroblasts (Fleischer et al., 2018) (see *Public datasets*) were retrieved using *fastq-dump* (version 2.9.3). All RNA-seq reads were aligned to the hg19 human reference genome using Tophat2 with the default parameter set (Kim et al., 2013). Reads with MAPQ score greater than 50 were used in downstream analyses. For each of the total 31,561 genes (see *Gene annotation*) for each
640 replicate, we computed (1) unnormalized RNA-seq read coverage, which was the sum of per-base read coverage in exons; and (2) RPKM (Reads Per Kilobase of transcript per Million mapped reads), which was the unnormalized RNA-seq read coverage divided by the read length (50 nt) and then by the sum of the exon size in kilobase and then by the total number of reads in million. The RPKM scores were Log_2-transformed (Log_2(RPKM+0.001)), z-normalized (for each sample), and then used in Principal
645 Component Analysis (PCA) using *prcomp* function (*stats* package version 3.3.2) in R. The PCA found that two data sets, s78 (normal fibroblast GM05381 by Fleischer et al.) and KI429 (normal fibroblast GM08398 by this study), did not cluster with other normal-fibroblast datasets (**Fig. S4D**). A retrospective assessment of the RNA quality of KI429 found a sign of RNA degradation. The datasets s78 and KI429 were excluded from the subsequent analyses.

650

LADs

LADs were defined using non-pS22-LMNA ChIP-seq data in BJ-5ta. The hg19 genome was segmented into 5-kb non-overlapping windows, and for each window, the sum of perbase read coverage (from replicate-combined reads) was computed for non-pS22-LMNA ChIP-seq and the corresponding input. The coverage was normalized by sequencing depth. The depth-normalized coverage was used to compute per-window $\log_2$ ratios of ChIP over input. We then created 100 kb windows with a 5-kb step genome-wide. For each 100-kb window, if every one of the 20 constituting 5-kb windows had a positive $\log_2$ ratio and the mean $\log_2$ ratios of the constituting 5-kb windows was greater than 0.5, this 100-kb window was further processed. The qualified 100-kb windows were merged if overlapping or touching. After filtering regions overlapping blacklisted regions (see *Blacklisted regions*), we obtained 2,178 regions which we defined as LADs in BJ-5ta (**Table S6**).

DNA motif analysis

To find DNA motifs *de novo*, 150-bp sequences centered around the summit of the top 500 high-confident (defined by p-values) pS22-LMNA-binding sites were analyzed by MEME (v4.10.0) (Machanick and Bailey, 2011) with the following parameters: minimum motif size, 6 bp; maximum motif size, 12 bp; and the expected motif occurrence of zero or one per sequence (*-mod zoops*) and with the 1st-order Markov model (i.e. the dinucleotide frequency) derived from the 73,933 ATAC-seq sites as the background. The top five overrepresented motifs were then processed by TOMTOM (v4.11.3) (Gupta et al., 2007; Tanaka et al., 2011) to identify known motifs that corresponded to the *de-novo* identified motifs from human HOCOMOCOv10 motif database (Kulakovskiy et al., 2018). At the q-value cutoff of less than 0.001, the *de-novo* identified motifs #1 (AP1), #2 (FOX) and #4 (RUNX) found the corresponding known motifs in the database. The location and frequency of the *de-novo* identified motifs within the all pS22-LMNA-binding sites (total 22,966) were determined by FIMO (v4.10.0) with p-value threshold less than 0.0001.

Upregulated and downregulated genes in progeria

To identify differentially expressed genes between progeria-patient fibroblasts and normal-individual fibroblasts, we applied DESeq2 (version 1.14.1) (Love et al., 2014) on the unnormalized RNA-seq read coverage for the total 31,561 genes (see *RNA-seq data processing*). To account for the variables due to
680 the study origins (**Fig. S4D**), we included the study origin annotation as an additive term in the DESeq2 model. We applied the cutoff of DESeq2-computed adjusted p-value smaller than 0.05 and absolute DESeq2-adjusted $\log_2$-fold change greater than 0.5. Among 11,613 protein coding genes that had the minimum RPKM score greater than 0.01 across all analyzed samples ("expressed genes"), 615 genes were defined as upregulated and 502 genes were defined as downregulated in progeria-patient
685 fibroblasts compared with normal-individual fibroblasts (**Table S11**).

Gained and lost pS22-LMNA-binding sites in progeria

We first generated a union set of pS22-LMNA-binding sites in normal-individual fibroblast GM07492 and progeria-patient fibroblast AG11498 by collecting pS22-LMNA-enriched sites from the two cell lines and
690 then merging neighboring summits if the distance between the summits was equal to or smaller than 200 bp. When summits were merged, the center of the region generated by the merged summits was assigned as the new summit. This resulted in 15323 union pLMNA-binding site summits (**Table S12**). The summits were then extended +/–500 bp, and the sum of per-base read coverage of pS22-LMNA ChIP-seq (reads extended to 200 bp) within the 1000-bp regions was computed for each replicate of the
695 normal and progeria fibroblasts (two replicates each). This coverage matrix was processed using DESeq2 (version 1.14.1) (Love et al., 2014) to identify pLMNA-binding sites with statistically-significant difference between the normal and progeria-patient fibroblast cell lines. At DESeq2-computed adjusted p-value < 0.05 and absolute $\log_2$-fold change > 0.5, we identified 2,796 sites whose pS22-LMNA signals were higher in progeria fibroblasts than in normal fibroblasts (gained pLMNA-binding sites) and 2,425
700 sites whose pS22-LMNA signals were higher in normal fibroblasts than in progeria fibroblasts (lost pLMNA-binding sites) (**Table S12**).

Gained and lost LADs in progeria

We first generated 5-kb windows genome-wide, and for each window and for each cell type (normal-
705 individual GM07492 and progeria-fibroblast AG11498), we computed the mean of the replicate-combined non-pS22-LMNA ChIP-seq log2-fold-enrichment scores within the window. The data was then quantile-normalized using *normalize.quantiles* function in the *preprocessCore* package (v1.36.0) in software R (Bolstad et al., 2003). From the normalized data, we identified: (1) seeds of lost LADs, which were 5-kb windows whose normal-fibroblast score was a positive number and whose progeria-fibroblast score was
710 a negative number; (2) seeds for gained LADs, which were 5-kb windows whose normal-fibroblast score was a negative number and whose progeria-fibroblast score was a positive number; and (3) seeds for steady LADs, which were 5-kb windows whose normal-fibroblast and progeria-fibroblast scores were both positive. For gained and lost LADs, the neighboring 5-kb seed windows were merged (individually for gained and lost LAD seeds) if they were located within 10 kb (i.e. a gap of two non-seed 5-kb windows
715 was allowed). For steady LADs, the seed 5-kb windows were merged if the neighboring seed windows were located within 5 kb (i.e. a gap of one non-seed 5-kb windows was allowed). Finally, the merged windows greater than 100 kb in size were isolated, and then those intersecting blacklisted regions (see *Blacklisted regions*) were filtered out. These processing resulted in 282 gained LADs, 353 lost LADs, and 2,100 steady LADs (**Table S13**).

720

Aggregate plot and heatmap

To generate aggregate plots and heatmaps for features, two data files were first generated: (a) a window file, which consists of, for each genomic feature, a set of fixed-size genomic windows that cover genomic intervals around the feature; and (b) a genome-wide signal file (in bedgraph format). For each genomic
725 window in the window file, all signals within that window were obtained from the signal file, and either mean or max of the signals or sum of the perbase signal ("area") were computed.

For the heatmaps and aggregate plots around pLMNA-binding sites or ATAC sites, a set of 250-bp windows with a 50-bp offset that covered a 10-kb region centered around the summit of these sites

was generated for each site. For each window, the mean of fold-enrichment score was computed from
730 replicate-combined input-normalized fold enrichment bedgraph files.

For the heatmaps of LADs, a set of 5-kb windows (without an offset) that covered the LAD body or the LAD body plus 250 kb downstream region was generated for each LAD. For each window, the mean of fold-enrichment score was computed from replicate-combined input-normalized fold enrichment bedgraph files.

735 For the heatmap of the differentially expressed genes, RPKM scores for the 11,613 expressed genes for the 26 RNA-seq data sets (12 normal fibroblasts and 14 progeria-patient fibroblasts) were $\log_{10}$-transformed and quantile-normalized using *normalize.quantiles* function in the *preprocessCore* package (v1.36.0) in R (Bolstad et al., 2003). These normalized scores were then processed using *ComBat* function in the *sva* package (v3.22.0) in R with the sample origin annotation as the batch to remove
740 (Johnson et al., 2007). The batch-normalized RPKM scores for the total 1,117 dysregulated genes in progeria fibroblasts were clustered and visualized using *pheatmap* function in the *pheatmap* package (v1.0.12) in R with the "correlation" clustering distance measurement method between sample clusters.

Gene ontology analysis

745 Gene ontology (GO) analyses were performed using Metascape (Tripathi et al., 2015). The input data type was Gencode 19 *Gene Symbol* (see *Gene annotation*). For background, the 11,613 protein-coding genes with reliable sequencing coverage were used (see *Differentially expressed genes*). Enrichment for "DisGeNet" terms (Piñero et al., 2017) was analyzed under the default parameter settings (minimum gene count 3, $P < 0.01$, enrichment over background >1.5).

750

Statistics

***Mann-Whitney U test*:** Throughout the paper, Mann-Whitney *U* test was used to assess statistical difference of numeric scores between two groups. The tests were performed using *wilcox.test* function with default parameters in R (*stats* package v3.3.2) under the null hypothesis that the score distributions

755 of the two groups under comparison were equal, with the alternative hypothesis that the two distributions were not equal.

One-sample t test: One-sample t-tests were performed using *t.test* function with default parameters in R (*stats* package v3.3.2) under the null hypothesis that the mean of the numeric vector equal to zero, with the alternative hypothesis that the mean is not equal to zero.

760 ***Fisher's exact test:*** Throughout the paper, Fisher's exact tests were used to assess the association between two features that were unambiguously and independently assigned to each data point in one data set. The tests were performed on a 2-by-2 contingency table using *fisher.test* function with default parameters in R (*stats* package v3.3.2) under the null hypothesis that the odds ratio is equal to 1, with alternative hypothesis that the odds ratio is not equal to 1.

765 ***Permutation test for chromatin state analysis of the 22,966 pLMNA-binding sites:*** For the 22,966 pLMNA-binding site summits (1 bp), a random set of 22,966 genomic locations was selected from the blacklisted-region-filtered genome using *shuffle* function in Bedtools (v2.25.0) (Quinlan and Hall, 2010) such that the chromosome distribution of the original 22,966 pLMNA-binding sites was maintained. This process was iterated 2,000 times. For each iteration, the total number of bases overlapped with a given

770 chromatin state was computed. For each chromatin state, the number of iterations in which the base coverage of permutated pLMNA-binding sites exceeded the actual base coverage of the 22,966 pLMNA-binding sites was counted. If this number is 0 (one-sided test for over-representation), we assigned empirical P-value of < 0.001. Essentially, the same computation was performed for 2,178 LADs, except that the random sets of LADs maintained the distribution of the original feature sizes.

775 ***GO-term enrichment***: P-values indicating GO-term enrichment were computed using Metascape (Tripathi et al., 2015), which uses a cumulative hypergeometric statistical test.

Public datasets

Assembly gaps

780 http://hgdownload.soe.ucsc.edu/goldenPath/hg19/database/gap.txt.gz

Blacklisted Regions

http://hgdownload.cse.ucsc.edu/goldenPath/hg19/encodeDCC/wgEncodeMapability/wgEncodeDacMapabilityConsensusExcludable.bed.gz

Chromatin annotation

785 http://egg2.wustl.edu/roadmap/data/byFileType/chromhmmSegmentations/ChmmModels/coreMarks/jointModel/final/E126_15_coreMarks_stateno.bed.gz

Genecode Release 19 Gene Model

http://hgdownload.cse.ucsc.edu/goldenPath/hg19/database/wgEncodeGencodeBasicV19.txt.gz

Progeria fibroblast RNA-seq datasets from Fleischer et al.

790 https://www.ncbi.nlm.nih.gov/geo/query/acc.cgi?acc=GSE113957

Data availability

Genomic datasets are available at Gene Expression Omnibus (http://www.ncbi.nlm.nih.gov/geo/) under the accession number GSE113354. All of the scripts used in this study will be deposited to a public github

795 website before publication.

SUPPLEMENTARY TABLES

All Supplementary Tables are presented in the tabs in the Excel spreadsheet.

800 Excel file Set1:

Table S1: Oligonucleotide sequences (Text)

Table S2: Normal and progeria fibroblast cell lines (Text)

Table S3: High-throughput sequencing data sets (Text)

Table S4: Blacklisted regions (UCSC Bed)

805

Excel file Set2:

Table S5: pS22-LMNA-binding sites in BJ-5ta (UCSC Bed)

Table S6: LADs in BJ-5ta (UCSC Bed)

Table S7: ATAC-seq peaks in BJ-5ta (UCSC Bed)

810

Excel file Set3:

Table S8: H3K27ac ChIP-seq peaks in BJ-5ta (UCSC Bed)

Table S9: H3K4me3 ChIP-seq peaks in BJ-5ta (UCSC Bed)

Table S10: c-Jun ChIP-seq peaks in BJ-5ta (UCSC Bed)

815

Excel file Set4:

Table S11: Differentially-expressed genes in progeria (UCSC Bed)

Table S12: Gained and lost pS22-LMNA-binding sites in progeria (UCSC Bed)

Table S13: Gained and lost LADs in progeria (UCSC Bed)

820

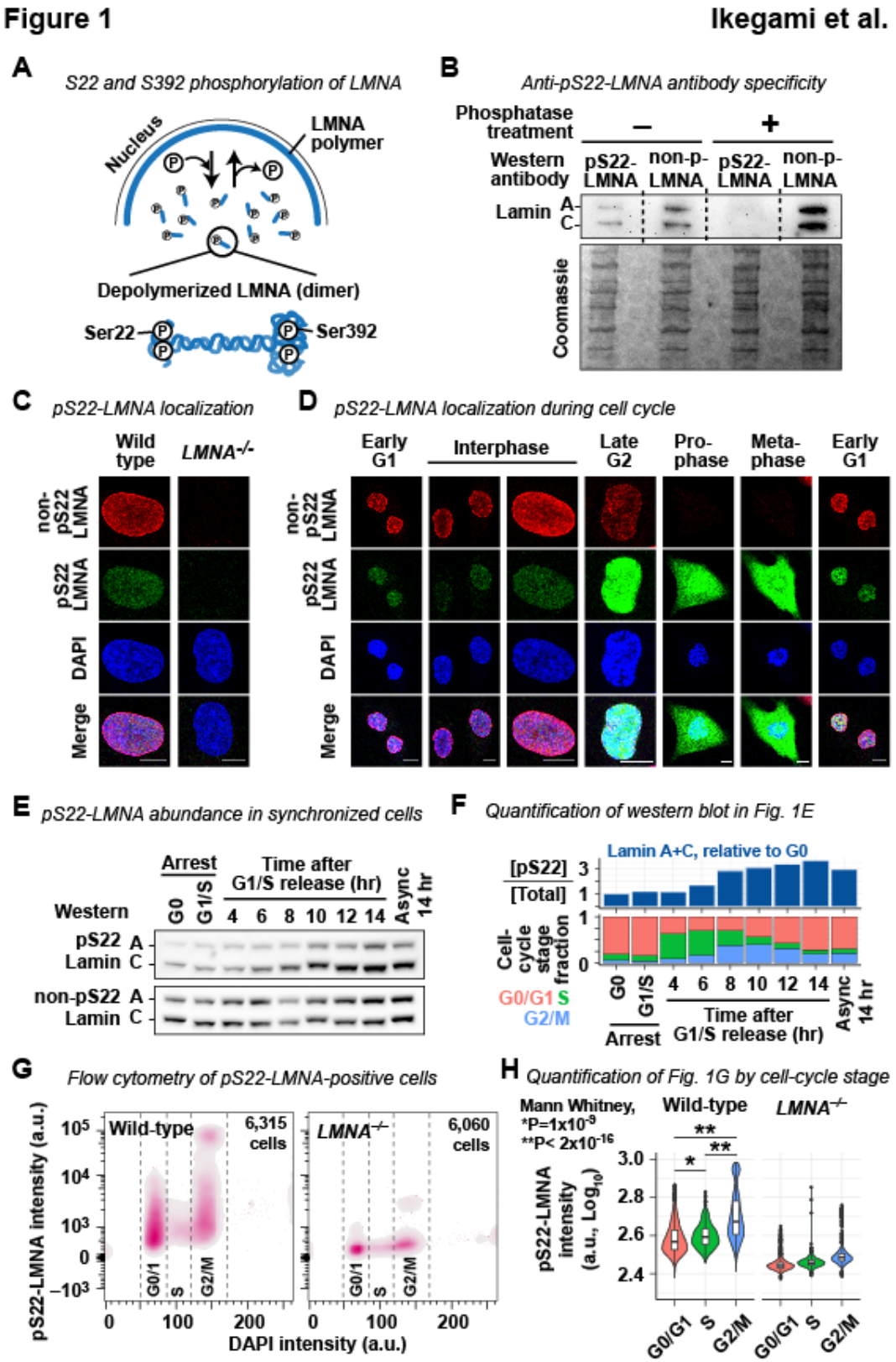

Figure 1. pS22-LMNA is localized in the interior of the nucleus throughout the cell cycle.
(A) Ser22 and Ser392 phosphorylation of LMNA trigger depolymerization.
825 **(B)** On-membrane Lambda protein phosphatase treatment of BJ-5ta cell extract followed by western blotting with anti-pS22- or anti-non-pS22-LMNA antibodies. Coomassie staining for loading control.

(C) Immunofluorescence for non-pS22- and pS22-LMNA. Wild-type, BJ-5ta. *LMNA*$^{-/-}$, BJ-5ta-derived *LMNA*$^{-/-}$ cells. Bar, 10 μm. See **Fig. S1A** for validation of BJ-5ta-derived *LMNA*$^{-/-}$ cells.
(D) Same as **(G)**, but wild-type BJ-5ta cells at specific cell-cycle stages are shown. Bar, 10 μm.
830 **(E)** pS22- or non-pS22-LMNA western blotting of cell-cycle synchronized BJ-5ta cells. See **Fig. S1B** for cell-cycle stage analysis and **Fig. S1C** for the entire blots.
(F) (Top) Quantification of western blot signals in **(E)**. [pS22], a sum of Lamin A and Lamin C band intensities on pS22-LMNA western blot. [Total], sum of Lamin A and Lamin C band intensities on pS22-LMNA western blot and those on non-pS22-LMNA western blot. (Bottom) Cell-cycle stage fraction at
835 each time point.
(G) Per-cell anti-pS22-LMNA antibody-staining intensity as a function of per-cell DAPI-staining intensity measured by flow cytometry. a.u., arbitary unit.
(H) Distribution of per-cell pS22-LMNA staining intensity analyzed in **(G)** for each cell-cycle stage. Overlaid boxplot indicates quartiles and 1.5x interquartile ranges (same applies to all other boxplots in
840 this paper).

Figure 2 **Ikegami et al.**

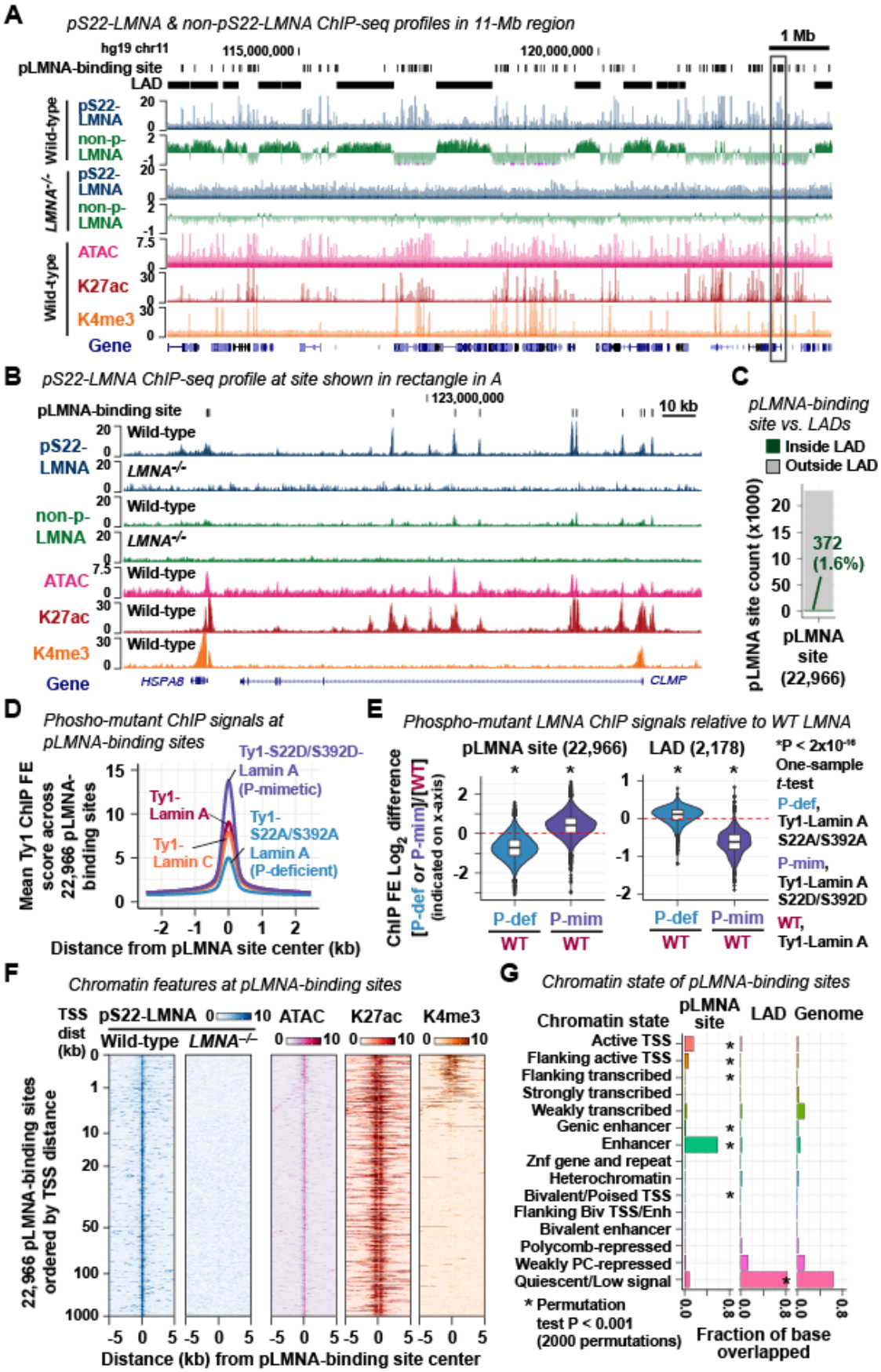

Figure 2. pS22-LMNA associates with putative enhancers genome-wide.

(A) Representative profiles of pS22-LMNA, non-pS22-LMNA, H3K27ac, and H3K4me3 ChIP-seq and
845 ATAC-seq fold-enrichment (FE) scores. ChIP FE scores are per-base ChIP read count normalized to input read count (Zhang et al., 2008). ATAC FE scores are per-base ATAC read count normalized to background read count estimated by the ATAC read distribution (Zhang et al., 2008). non-pS22-LMNA profiles are in the $\log_2$ scale to visualize the bimodal lamina association profile. LAD, lamina-associated domain. See **Fig. S2A–D** for additional characterization of pLMNA-binding sites.

850 **(B)** Genomic region shown in rectangle in **(A)**. The non-pS22-LMNA profiles are in the linear scale for a direct comparison with pS22-LMNA profiles.

(C) Number of pLMNA-binding sites inside or outside of the 2,178 LADs. LADs are defined by non-pS22-LMNA ChIP-seq.

(D) Mean Ty1 ChIP-seq FE score across 22,966 pLMNA-binding sites in BJ-5ta cells overexpressing
855 Ty1-tagged Lamin A, Lamin C, phospho-deficient Lamin A-S22A/S392, or phospho-mimetic Lamin A-S22D/S392D. See **Fig. S2E** for their ChIP-seq profiles.

(E) Log_2 difference of Ty1 ChIP-seq FE scores between phospho-mutant LMNA and wild-type LMNA at the 22,966 pLMNA-binding sites (left) or at the 2,178 LADs (right). Red dashed line indicates Log_2 score difference equals 0 for reference.

860 **(F)** pS22-LMNA ChIP-seq, ATAC-seq, H3K27ac ChIP-seq, and H3K4me3 ChIP-seq FE scores at the 22,966 pLMNA-binding sites. See **Fig. S3** for comparison of peak locations. TSS dist, distance from pLMNA-binding site center to the closest transcription start site.

(G) Chromatin states of the 22,966 pLMNA-binding sites and the 2,178 LADs. For each chromatin state annotation, the fraction of the bases overlapping the annotation is plotted. The chromatin state
865 annotations are defined in normal dermal fibroblasts (Roadmap Epigenomics Consortium et al., 2015).

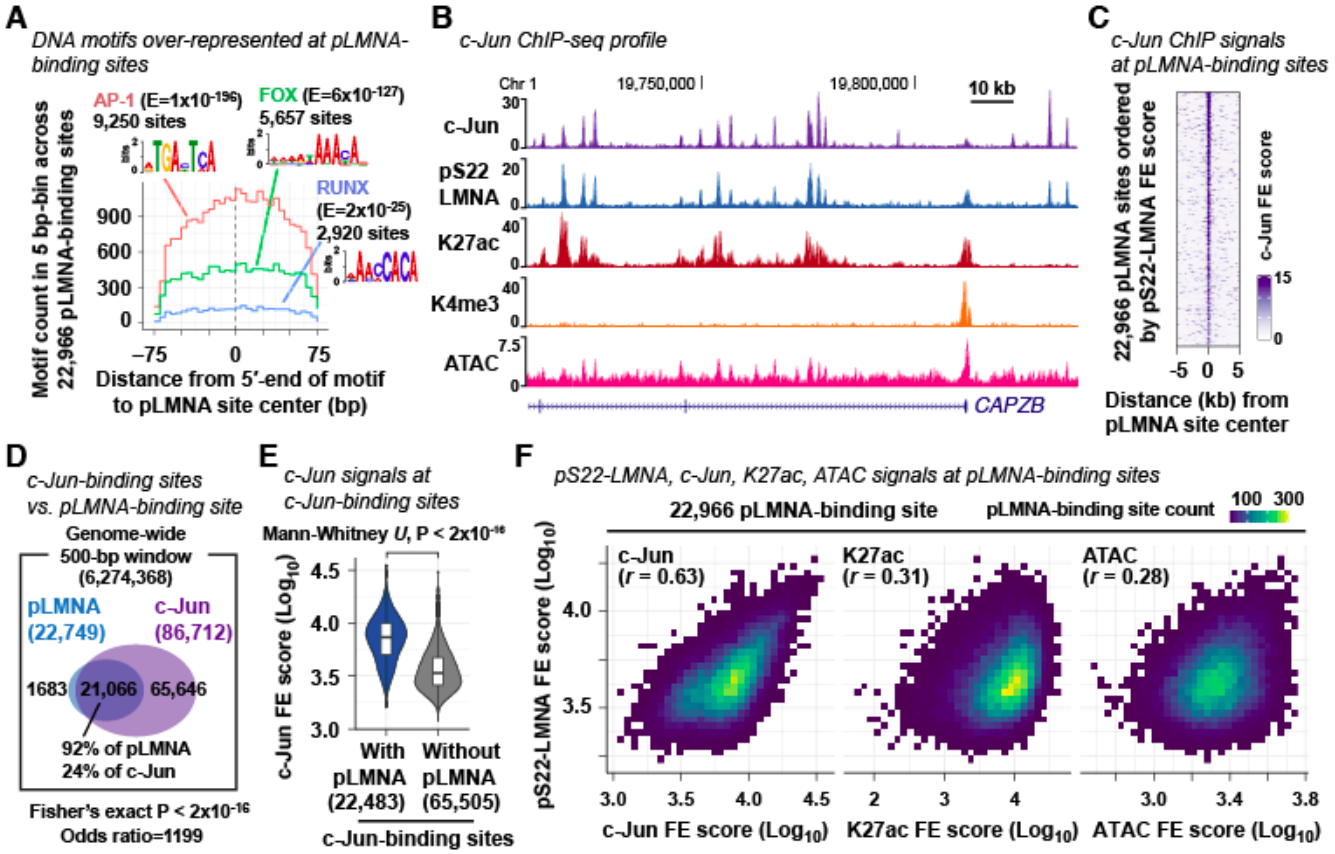

Figure 3. pS22-LMNA association and c-Jun association are strongly correlated at pLMNA-binding sites.

(A) Frequency of DNA motifs within the 22,966 pLMNA-binding sites. E, motif occurence probability score in *de novo* DNA motif search (Machanick and Bailey, 2011).

(B) A representative profile of c-Jun ChIP-seq fold-enrichment (FE) scores. c-Jun is the AP1 transcription factor. pS22-LMNA, H3K27ac, and H3K4me3 ChIP-seq profiles and ATAC-seq profile are shown for comparison.

(C) c-Jun ChIP-seq FE scores at the 22,966 pLMNA-binding sites.

(D) Comparison of pLMNA-binding site location and c-Jun-binding site location. Number indicates the number of 500-bp windows that overlap pLMNA-binding sites and/or c-Jun-binding sites.

(E) Sum of c-Jun FE scores within +/–250 bp of c-Jun-binding site center. c-Jun-binding sites are grouped by the presence or absense of overlapping pLMNA-binding sites.

(F) Two-dimensional histogram for the 22,966 pLMNA-binding sites, binned by the FE score of c-Jun, H3K27ac, or ATAC (x-axis) and the FE score of pS22-LMNA (y-axis). One square, one bin, with color grade representing the number of pLMNA-binding sites within the bin. *r*, pearson correlation coefficient.

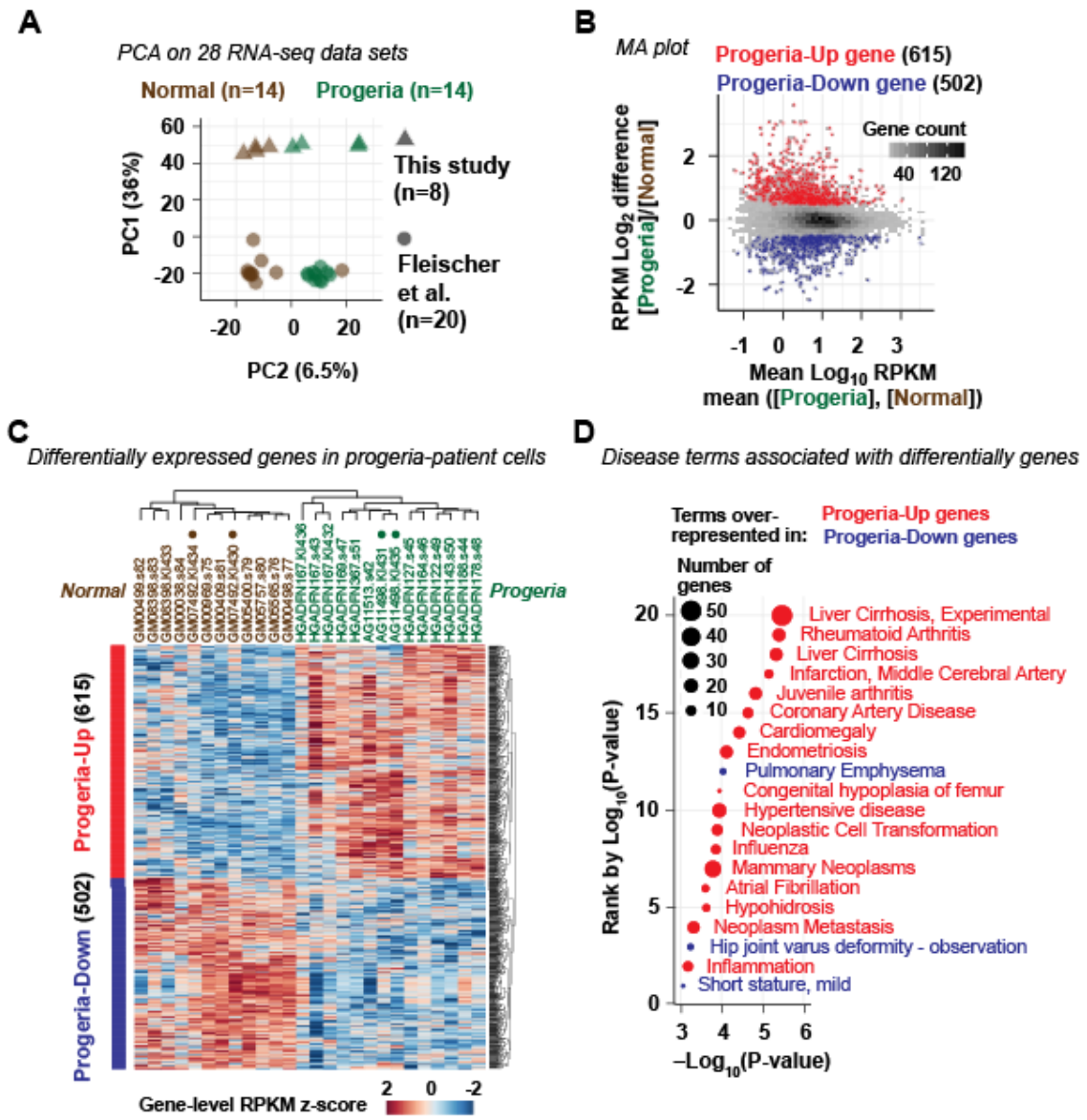

Figure 4. Genes abnormally up-regulated in progeria fibroblasts are relevant to progeria phenotypes.

(A) Principal component analysis (PCA) on RNA-seq data sets of primary fibroblasts derived from normal individuals (14 data sets) and progeria patients (14 data sets). Percentage indicates the proportion of variance explained by the principal component. See **Figure S4** for additional PCA analyses and sample details.

(B) MA plot comparing mean RPKMs between 14 progeria fibroblast RNA-seq data sets and 12 normal fibroblast RNA-seq data sets.

(C) Hierachical clustering of progeria-up and progeria-down genes (row) and normal and progeria fibroblast RNA-seq data sets (column). Solid circles indicate normal GM07492 cells and progeria AG11497 cells, used in the analyses of LADs and pLMNA-binding sites.

(D) DisGeNet-curated disease terms over-represented among progeria-up (red) and progeria-down genes (blue). All terms with P-values smaller than 0.001 are shown.

905

Figure 5 **Ikegami et al.**

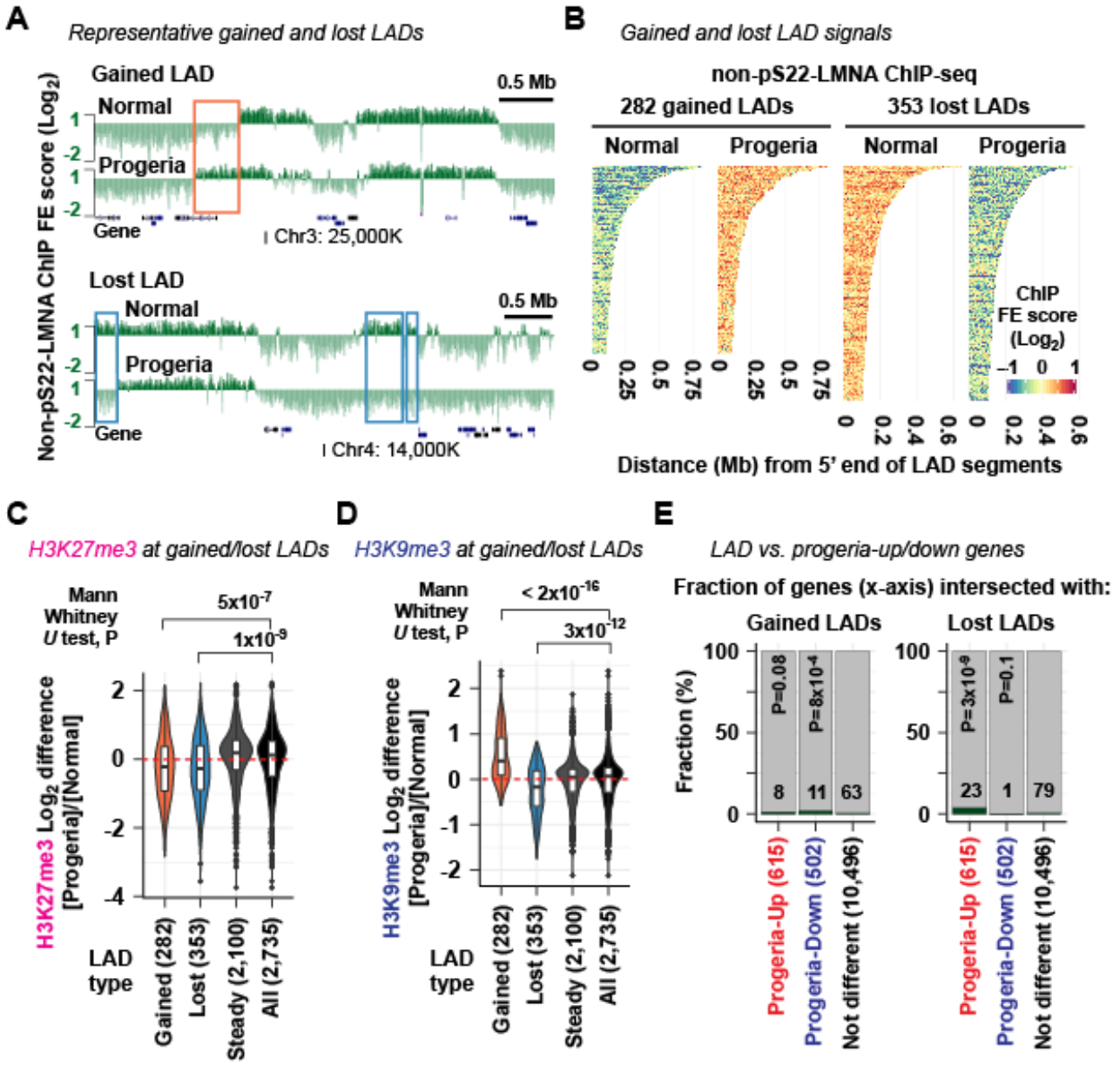

Figure 5. LAD alterations do not explain the majority of gene expression changes in progeria.
(A) Non-pS22-LMNA ChIP-seq fold-enrichment (FE) score tracks ($\log_2$ scale on y axis) highlighting representative gained and lost LADs. Normal, GM07492 normal fibroblst. Progeria, AG11498 progeria
910 fibroblast. Additional representative gained and lost LADs are shown in **Figure S5**.
(B) Non-pS22-LMNA ChIP-seq FE score in the normal GM07492 and progeria AG11498 fibroblasts at the 289 gained LADs and 361 lost LADs.
(C) H3K27me3 ChIP-seq FE $\log_2$ difference between normal and progeria fibroblasts. Normal, FE score of GM07492. Progeria, FE score of AG11498. Red dashed line, Log_2 difference equals 0 for reference.
915 **(D)** Same as **(C)**, but H3K9me3 $\log_2$ difference is shown.
(E) Fraction of progeria-up and progeria-down genes whose gene body or upstream 100-kb region intersected with gained LADs (left) or lost LADs (right). P, Fisher's exact test P value comparing the fraction of progeria-up/down genes with that of all genes.

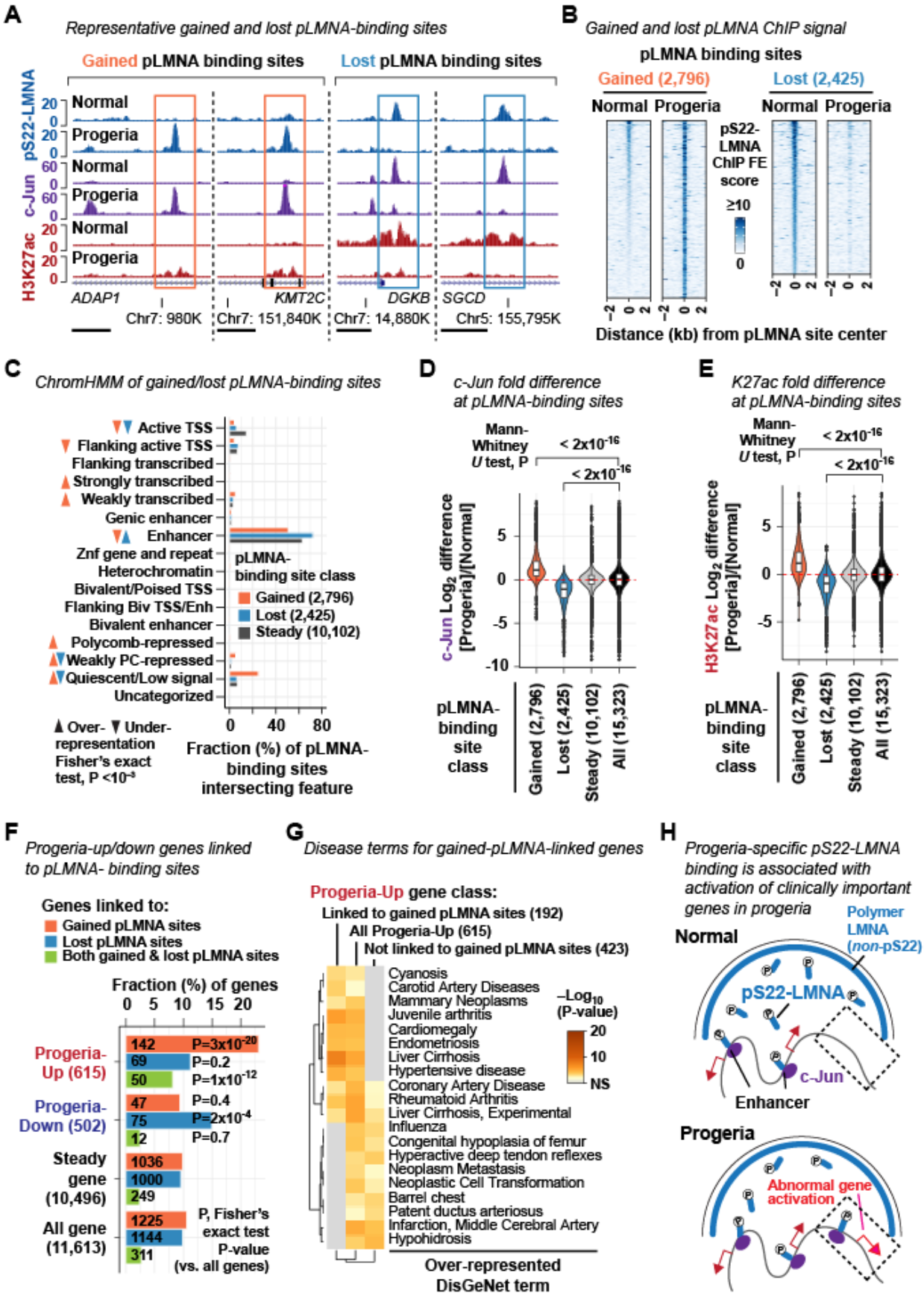
A
Representative gained and lost pLMNA-binding sites
Gained pLMNA binding sites
Lost pLMNA binding sites
pS22-LMNA
c-Jun
H3K27ac
Normal
Progeria
ADAP1
KMT2C
DGKB
SGCD
Chr7: 980K
Chr7: 151,840K
Chr7: 14,880K
Chr5: 155,795K
B
Gained and lost pLMNA ChIP signal
pLMNA binding sites
Gained (2,796)
Lost (2,425)
Normal Progeria
pS22-LMNA ChIP FE score
≥10
0
Distance (kb) from pLMNA site center
C
ChromHMM of gained/lost pLMNA-binding sites
Active TSS
Flanking active TSS
Flanking transcribed
Strongly transcribed
Weakly transcribed
Genic enhancer
Enhancer
Znf gene and repeat
Heterochromatin
Bivalent/Poised TSS
Flanking Biv TSS/Enh
Bivalent enhancer
Polycomb-repressed
Weakly PC-repressed
Quiescent/Low signal
Uncategorized
pLMNA-binding site class
Gained (2,796)
Lost (2,425)
Steady (10,102)
Over- Under-representation Fisher's exact test, P <10⁻⁵
Fraction (%) of pLMNA-binding sites intersecting feature
D
c-Jun fold difference at pLMNA-binding sites
Mann-Whitney U test, P
< 2x10⁻¹⁶
c-Jun Log2 difference [Progeria]/[Normal]
pLMNA-binding site class
Gained (2,796)
Lost (2,425)
Steady (10,102)
All (15,323)
E
K27ac fold difference at pLMNA-binding sites
H3K27ac Log2 difference [Progeria]/[Normal]
F
Progeria-up/down genes linked to pLMNA- binding sites
Genes linked to:
Gained pLMNA sites
Lost pLMNA sites
Both gained & lost pLMNA sites
Fraction (%) of genes
Progeria-Up (615)
Progeria-Down (502)
Steady gene (10,496)
All gene (11,613)
P=3x10⁻²⁰
P=0.2
P=1x10⁻¹²
P=0.4
P=2x10⁻⁴
P=0.7
P, Fisher's exact test P-value (vs. all genes)
G
Disease terms for gained-pLMNA-linked genes
Progeria-Up gene class:
Linked to gained pLMNA sites (192)
All Progeria-Up (615)
Not linked to gained pLMNA sites (423)
Cyanosis
Carotid Artery Diseases
Mammary Neoplasms
Juvenile arthritis
Cardiomegaly
Endometriosis
Liver Cirrhosis
Hypertensive disease
Coronary Artery Disease
Rheumatoid Arthritis
Liver Cirrhosis, Experimental
Influenza
Congenital hypoplasia of femur
Hyperactive deep tendon reflexes
Neoplasm Metastasis
Neoplastic Cell Transformation
Barrel chest
Patent ductus arteriosus
Infarction, Middle Cerebral Artery
Hypohidrosis
−Log10 (P-value)
NS
Over-represented DisGeNet term
H
Progeria-specific pS22-LMNA binding is associated with activation of clinically important genes in progeria
Normal
Polymer LMNA (non-pS22)
pS22-LMNA
c-Jun
Enhancer
Progeria
Abnormal gene activation

Figure 6. New pLMNA-binding sites emerged in progeria are associated with up-regulation of genes relevant to progeria phenotypes.

(A) pS22-LMNA ChIP-seq fold-enrichment (FE) score tracks highlighting representative gained and lost pLMNA-binding sites. Normal, GM07492 normal fibroblst. Progeria, AG11498 progeria fibroblast. Horizontal bar, 2 kb. See **Figure S6** for additional characterization of gained and lost pLMNA-binding sites.

(B) pS22-LMNA ChIP-seq FE score in the normal GM07492 and progeria AG11498 fibroblasts at the 2,796 gained and 2,425 lost pLMNA-binding sites.

(C) Fraction of gained, lost, or all pLMNA-binding sites intersecting chromatin state annotations. Fisher's exact test is used to compare fraction of gained or lost pLMNA-binding sites with that of all pLMNA-binding sites.

(D) c-Jun ChIP-seq FE score difference between normal and progeria fibroblasts. [Normal], FE score of GM07492. [Progeria], FE score of AG11498. Red dashed line, Log_2 difference equals 0 for reference.

(E) Same as **(D)**, but fold-enrichment scores of H3K27ac ChIP-seq are shown.

(**F**) Fraction of progeria-up and progeria-down genes linked to gained and/or lost pLMNA-binding sites. Fractions within steady genes and all genes are shown for reference. Genes are linked to pLMNA-binding sites when pLMNA-binding sites reside in the gene body and/or the upstream 100-kb region.

(**G**) DisGeNet-curated disease terms over-represented among progeria-up genes linked to gained pLMNA-binding sites (192), those not linked to gained pLMNA-binding site (423), and all progeria-up genes (615).

(H) Summary. In normal fibroblasts, pS22-LMNA associates with putative active enhancers. In progeria, gains of pLMNA-binding sites in abnormal locations accompany activation of genes relevant to progeria phenotypes.

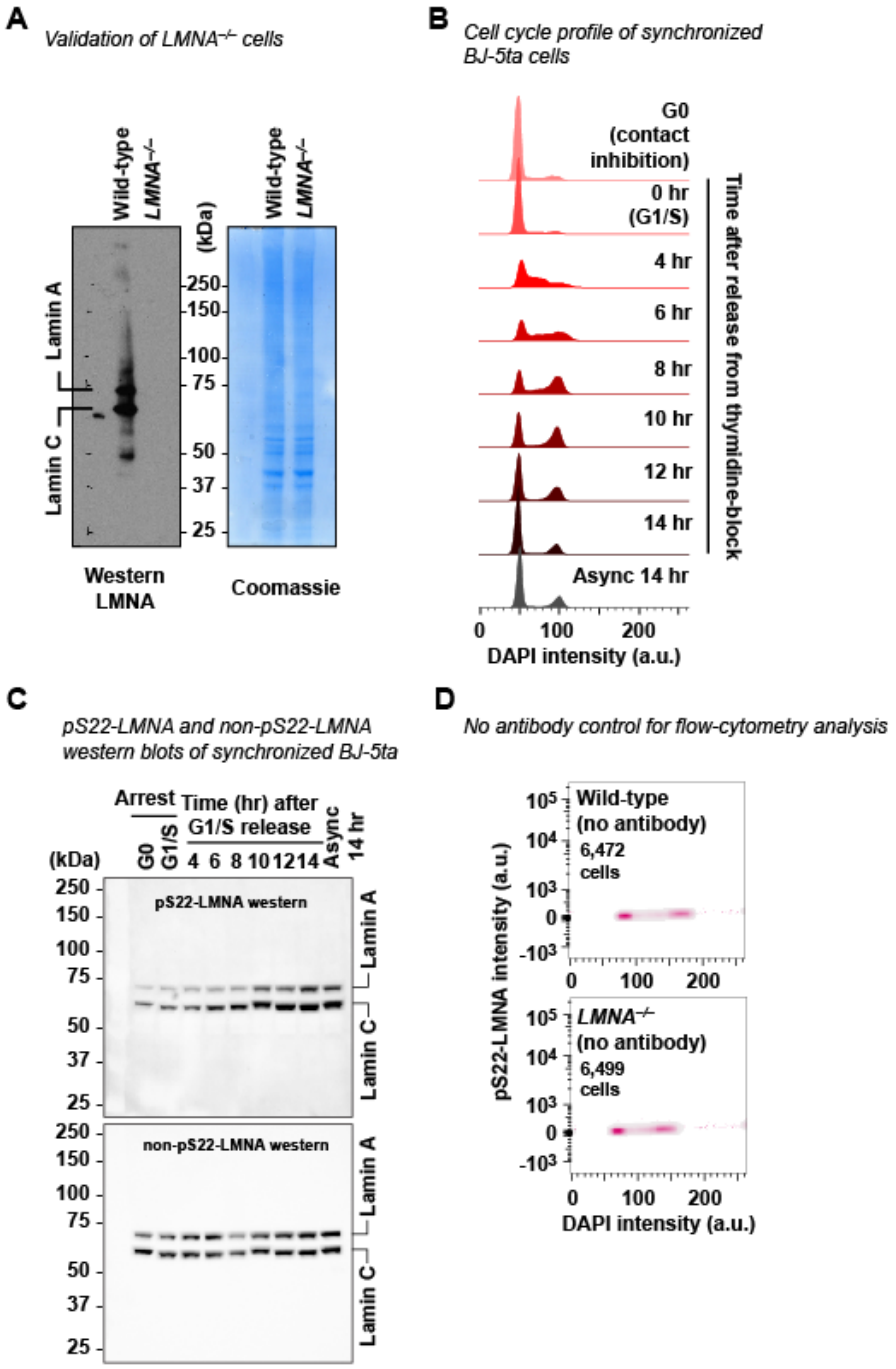

Figure S1. Characterization of pS22-LMNA (related to Figure 1)
(A) LMNA western blots of wild-type BJ-5ta and BJ-5ta-derived *LMNA*−/− cells. LMNA proteins are absent in *LMNA*−/− cells. An anti-LMNA antibody for aa231-340 (Santa Cruz H-110) is used for western. Coomassie staining of the membrane for loading control.
(B) Histogram of per-cell DAPI intensity used to determine cell-cycle stages of synchronized wild-type BJ-5ta cells in **Fig. 1E & F**.

(C) The entire pS22- and non-pS22-LMNA western blots of synchronized wild-type BJ-5ta cells, part of which are shown in **Fig. 1E**. The blot does not detect degradation products of LMNA in the pS22-LMNA western.

(D) No antibody control for the flow cytometry analysis in **Fig. 1G**.

960

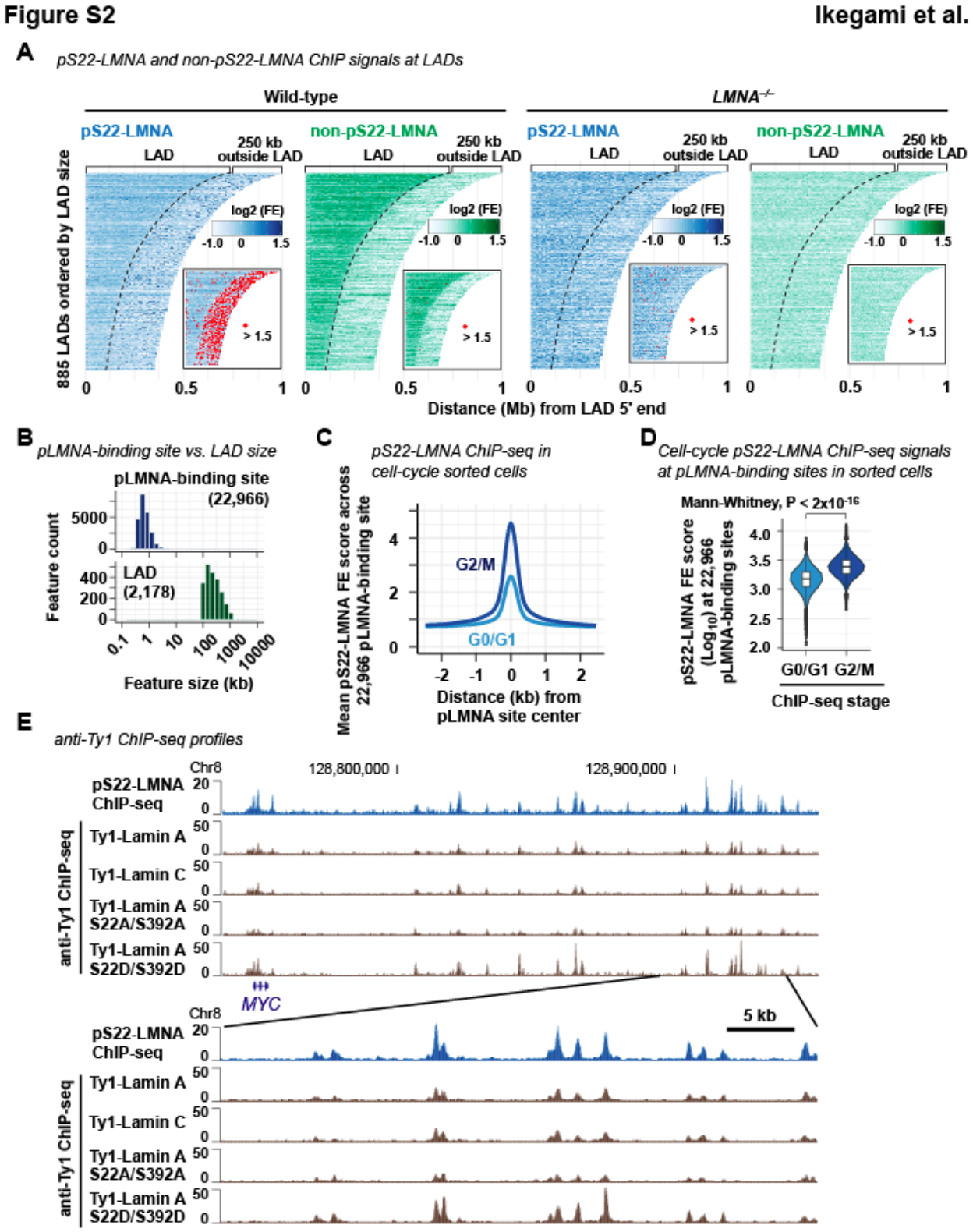

Figure S2. Characterization of pS22-LMNA-binding sites (related to Figure 2)
(A) pS22-LMNA and non-pS22-LMNA ChIP-seq fold-enrichment (FE) scores at LADs. LADs are defined by non-pS22-LMNA ChIP-seq (see Methods). A subset of LADs (885 of total 2,178) that do not have adjacent LADs within 250 kb downstream of LADs are shown. Inset shows locations of strong ChIP-seq FE scores, most of which are pLMNA-binding sites (marked in red).
(B) Histogram of feature size of pLMNA-binding sites and LADs.

(C) Mean pS22-LMNA ChIP-seq FE scores across the 22,966 pLMNA-binding sites in BJ-5ta cells sorted
970 for the G0/G1 or G2/M cell-cycle stage.
(D) Distribution of pS22-LMNA FE scores at 22,966 pLMNA-binding sites (sum of the score within +/– 250 bp of pLMNA-binding site center) in BJ-5ta cells sorted for the G0/G1 or G2/M cell-cycle stage.
(E) A representative region showing profiles for anti-Ty1 ChIP-seq FE scores. pS22-LMNA ChIP-seq profile is shown for comparison.
975

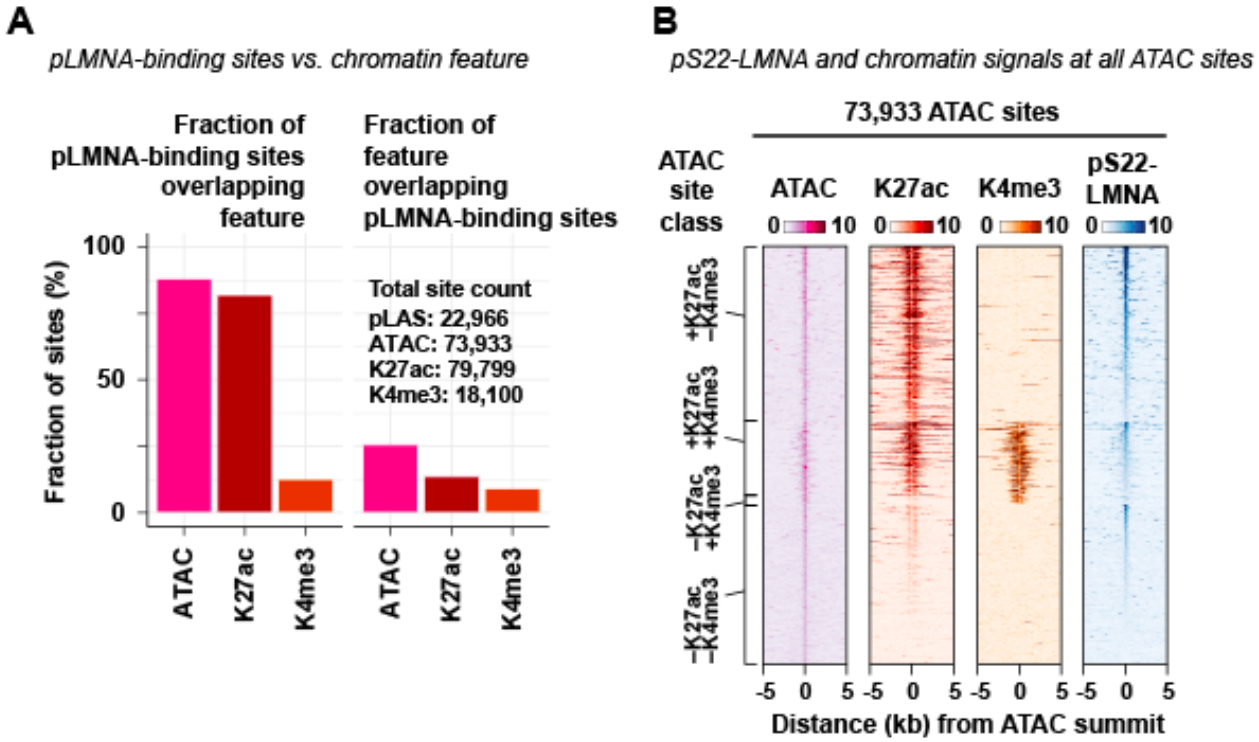

Figure S3. Chromatin characteristics of pLMNA-binding sites (related to Figure 2)
(A) Fraction of the 22,966 pLMNA-binding sites that overlap ATAC-seq-defined accessible sites, H3K27ac ChIP-seq peaks, or H3K4me3 ChIP-seq peaks in BJ-5ta.
(B) ATAC-seq, H3K27ac ChIP-seq, H3K4me3 ChIP-seq, and pS22-LMNA ChIP-seq fold-enrichment (FE) scores at the 73,933 ATAC-seq-defined accessible sites in BJ-5ta.

Figure S4 **Ikegami et al.**

A

RNA-seq data sets used in this study

Data ID	Donor type	Cell line name	Data source
KI429	Normal	GM08398	This study
KI430	Normal	GM07492	This study
KI433	Normal	GM08398	This study
KI434	Normal	GM07492	This study
s75	Normal	GM00969	Fleischer et al.
s76	Normal	GM05565	Fleischer et al.
s77	Normal	GM00498	Fleischer et al.
s78	Normal	GM05381	Fleischer et al.
s79	Normal	GM05400	Fleischer et al.
s80	Normal	GM05757	Fleischer et al.
s81	Normal	GM00409	Fleischer et al.
s82	Normal	GM00499	Fleischer et al.
s83	Normal	GM08398	Fleischer et al.
s84	Normal	GM00038	Fleischer et al.
KI431	HGPS	AG11498	This study
KI432	HGPS	HGADFN167	This study
KI435	HGPS	AG11498	This study
KI436	HGPS	HGADFN167	This study
s42	HGPS	AG11513	Fleischer et al.
s43	HGPS	HGADFN167	Fleischer et al.
s44	HGPS	HGADFN188	Fleischer et al.
s45	HGPS	HGADFN127	Fleischer et al.
s46	HGPS	HGADFN164	Fleischer et al.
s47	HGPS	HGADFN169	Fleischer et al.
s48	HGPS	HGADFN178	Fleischer et al.
s49	HGPS	HGADFN122	Fleischer et al.
s50	HGPS	HGADFN143	Fleischer et al.
s51	HGPS	HGADFN367	Fleischer et al.

Norma, normal individual
HGPS, patients with Hutchinson-Gilford Progeria Syndrome
Fleischer et al, *Genome Biology* (2018) PMID: 30567591

B

Beta-galactosidase assay for senescence evaluation

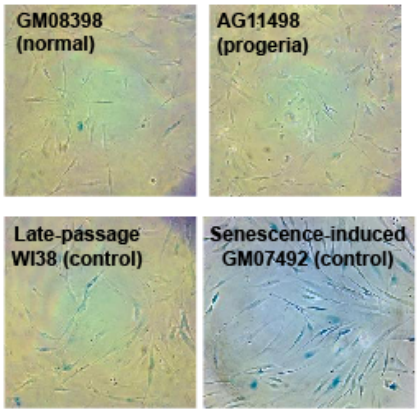

C

Quantification of beta-galactosidase assay

	Cell line	Condition	Positive cell %	Total cell count
Control	WI38	Early passage (PD25)	0%	206
	WI38	Late passage (PD41)	75%	156
	WI38	400 μM H_2O_2 (induced)	83%	151
	GM07	300 μM H_2O_2 (induced)	47%	201
Normal	GM07	Upon harvest	0.5%	195
	GM08	Upon harvest	2%	206
Progeria	AG11	Upon harvest	3%	206
	HG16	Upon harvest	1.5%	201

D

Principal component analysis of 28 RNA-seq data sets with data ID annotation

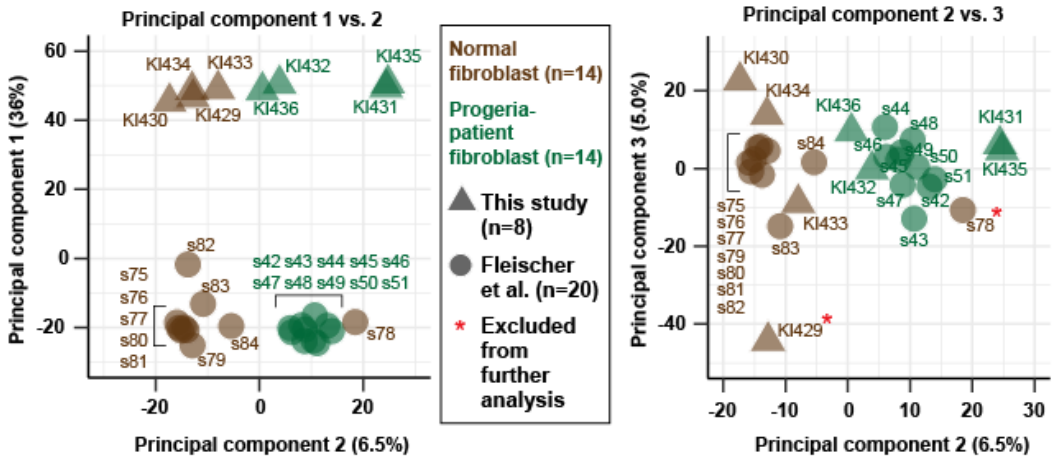

985

Figure S4. RNA-seq in progeria-patient fibroblasts (related to Figure 4)
(A) The 28 RNA-seq datasets used in this study.
(B) Representative images of beta-galactosidase assay evaluating the extent of cell senescence.
990 **(C)** Quantification of beta-galactosidase assay. Early-passage WI38 fibroblast serves as a negative control. Late-passage WI38 serves as a positive control. WI38 and GM07492 cells treated with H_2O_2 serve as additional positive controls. Cell line notation: GM08, GM08398. GM07, GM07492. AG11, AG11498. HG16, HGADFN167.

(D) Principal component analyses on RNA-seq RPKM for all 31,561 genes (see *Gene annotation* in
995 **Methods**). The left panel without data ID annotation is shown in **Figure 4A**.

Figure S5 **Ikegami et al.**

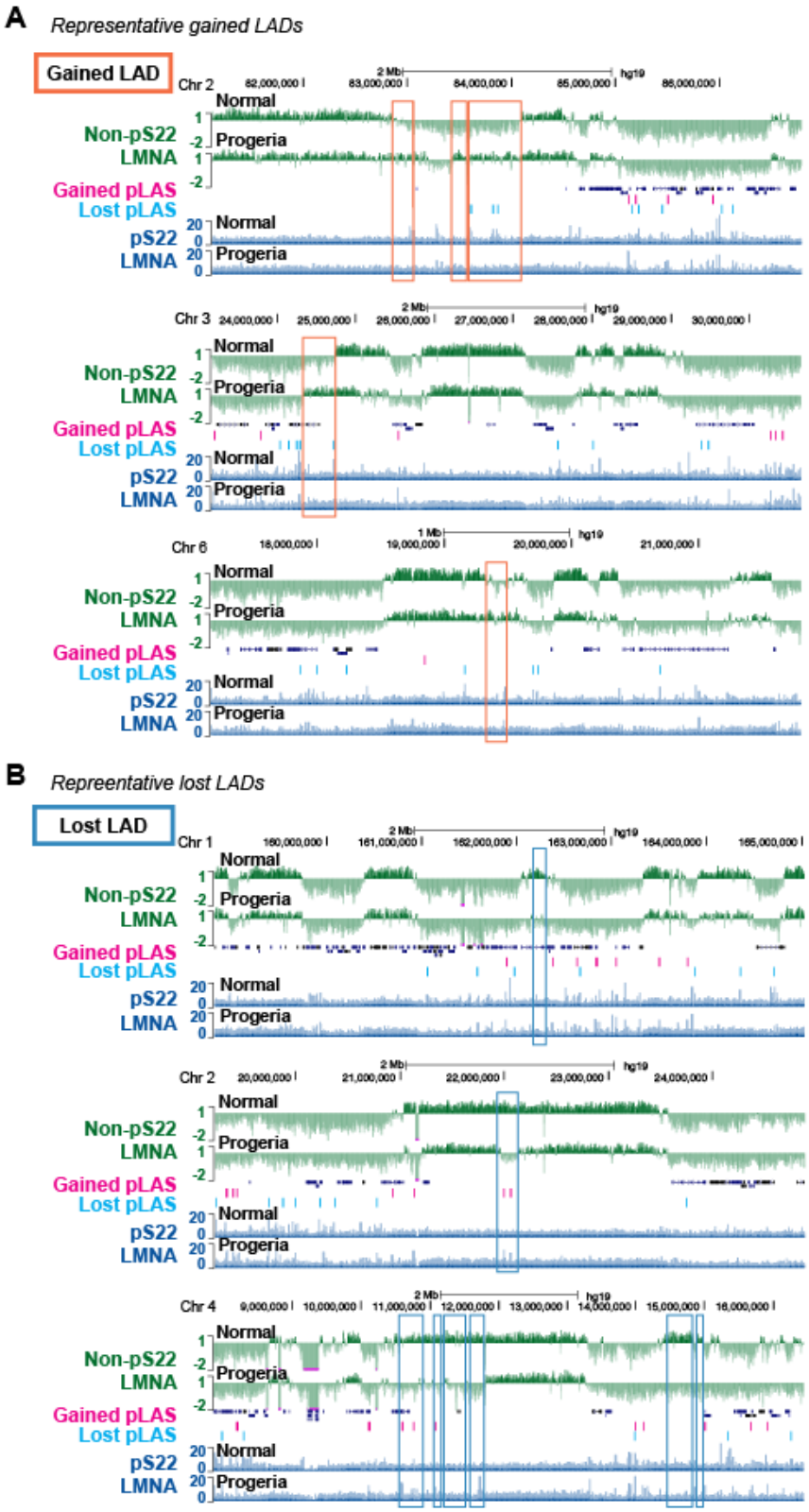

1000

Figure S5. Representative gained and lost LADs (related to Figure 5)
(A) Non-pS22-LMNA and pS22-LMNA ChIP-seq fold-enrichment (FE) score tracks. Rectangle, gained LADs. Non-pS22-LMNA profiles are in the $\log_2$ scale to visualize the bimodal lamina association profile.

(B) Same as **(A)**, but rectangles indicate lost LADs.

1005

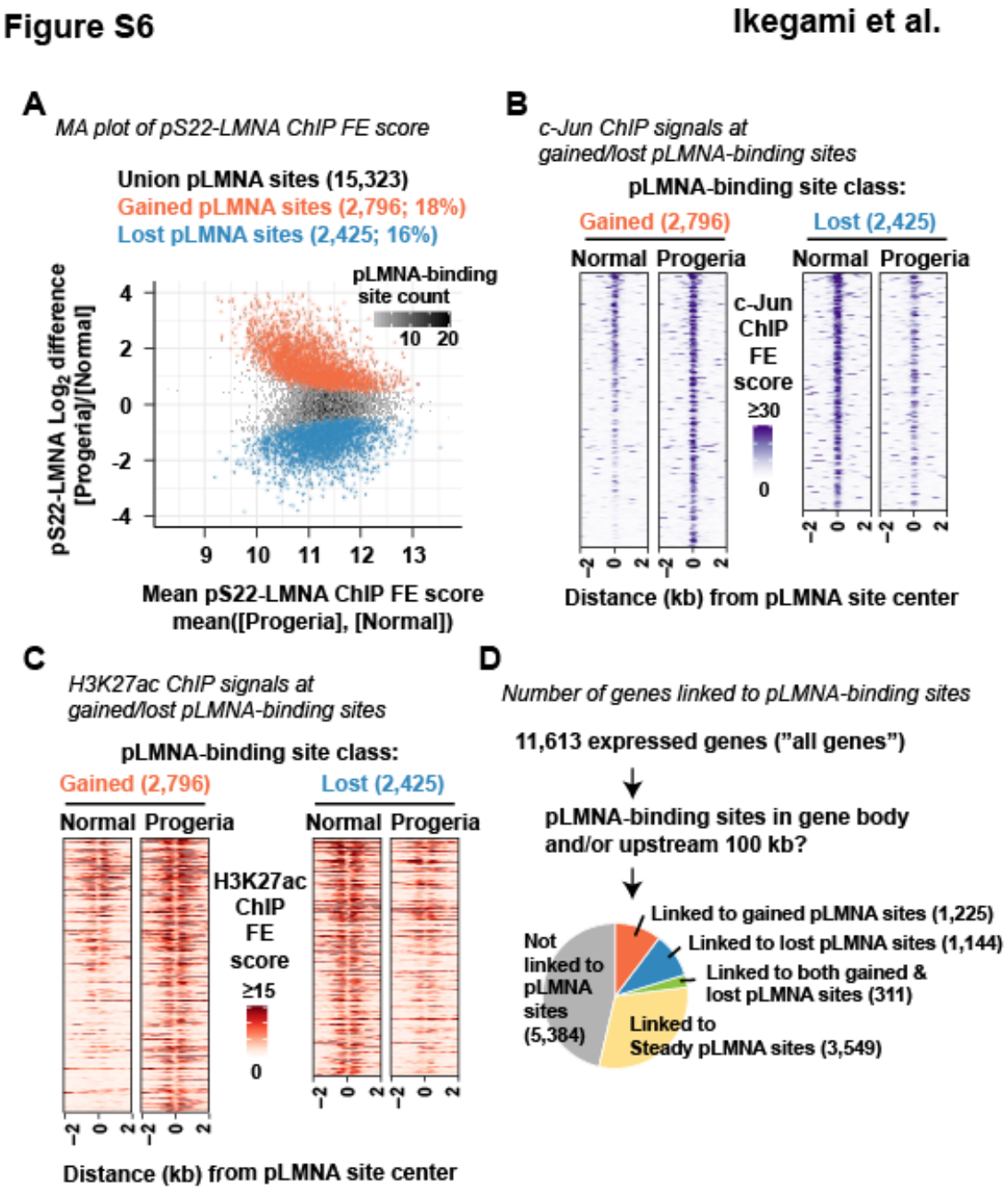

Figure S6. Gained and lost pLMNA-binding sites in progeria-patient fibroblasts (related to Figure 6)

(A) MA plot for the 15,323 union pLMNA-binding sites, highlighting gained and lost pLMNA-binding sites. [Normal], pS22-LMNA ChIP fold-enrichment score (FE) of normal fibroblast GM07492. [Progeria], pS22-LMNA ChIP FE of progeria fibroblast AG11498.

(B) c-Jun ChIP-seq FE score distribution around gained pLMNA-binding sites and lost pLMNA-binding sites.

(C) H3K27ac ChIP-seq FE score distribution around gained pLMNA-binding sites and lost pLMNA-binding sites.

(D) Number and fraction of genes linked to gained, lost, and steady pLMNA-binding sites.

REFERENCES

Aebi, U., Cohn, J., Buhle, L., and Gerace, L. (1986). The nuclear lamina is a meshwork of intermediate-type filaments. Nature *323*, 560–564.

Amendola, M., and van Steensel, B. (2015). Nuclear lamins are not required for lamina-associated domain organization in mouse embryonic stem cells. EMBO Rep. *16*, 610–617.

Barboro, P., D'Arrigo, C., Diaspro, A., Mormino, M., Alberti, I., Parodi, S., Patrone, E., and Balbi, C. (2002). Unraveling the organization of the internal nuclear matrix: RNA-dependent anchoring of NuMA to a lamin scaffold. Exp. Cell Res. *279*, 202–218.

Bolstad, B.M., Irizarry, R.A., Astrand, M., and Speed, T.P. (2003). A comparison of normalization methods for high density oligonucleotide array data based on variance and bias. Bioinformatics *19*, 185–193.

Bridger, J.M., Kill, I.R., O'Farrell, M., and Hutchison, C.J. (1993). Internal lamin structures within G1 nuclei of human dermal fibroblasts. J. Cell Sci. *104 (Pt 2)*, 297–306.

Broers, J.L., Machiels, B.M., van Eys, G.J., Kuijpers, H.J., Manders, E.M., van Driel, R., and Ramaekers, F.C. (1999). Dynamics of the nuclear lamina as monitored by GFP-tagged A-type lamins. J. Cell Sci. *112 (Pt 20)*, 3463–3475.

Bruston, F., Delbarre, E., Ostlund, C., Worman, H.J., Buendia, B., and Duband-Goulet, I. (2010). Loss of a DNA binding site within the tail of prelamin A contributes to altered heterochromatin anchorage by progerin. FEBS Lett. *584*, 2999–3004.

Buxboim, A., Swift, J., Irianto, J., Spinler, K.R., Dingal, P.C.D.P., Athirasala, A., Kao, Y.-R.C., Cho, S., Harada, T., Shin, J.-W., et al. (2014). Matrix elasticity regulates lamin-A,C phosphorylation and turnover with feedback to actomyosin. Curr. Biol. *24*, 1909–1917.

Csoka, A.B., English, S.B., Simkevich, C.P., Ginzinger, D.G., Butte, A.J., Schatten, G.P., Rothman, F.G., and Sedivy, J.M. (2004). Genome-scale expression profiling of Hutchinson-Gilford progeria syndrome reveals widespread transcriptional misregulation leading to mesodermal/mesenchymal defects and accelerated atherosclerosis. Aging Cell *3*, 235–243.

Dechat, T., Gesson, K., and Foisner, R. (2010a). Lamina-independent lamins in the nuclear interior serve important functions. Cold Spring Harb. Symp. Quant. Biol. *75*, 533–543.

Dechat, T., Adam, S.A., Taimen, P., Shimi, T., and Goldman, R.D. (2010b). Nuclear lamins. Cold Spring Harb. Perspect. Biol. *2*, a000547–a000547.

Dittmer, T.A., and Misteli, T. (2011). The lamin protein family. Genome Biol. *12*, 222.

Eriksson, M., Brown, W.T., Gordon, L.B., Glynn, M.W., Singer, J., Scott, L., Erdos, M.R., Robbins, C.M., Moses, T.Y., Berglund, P., et al. (2003). Recurrent de novo point mutations in lamin A cause Hutchinson-Gilford progeria syndrome. Nature *423*, 293–298.

Finlan, L.E., Sproul, D., Thomson, I., Boyle, S., Kerr, E., Perry, P., Ylstra, B., Chubb, J.R., and Bickmore, W.A. (2008). Recruitment to the nuclear periphery can alter expression of genes in human cells. PLoS Genet. *4*, e1000039.

Fleischer, J.G., Schulte, R., Tsai, H.H., Tyagi, S., Ibarra, A., Shokhirev, M.N., Huang, L., Hetzer, M.W., and Navlakha, S. (2018). Predicting age from the transcriptome of human dermal fibroblasts. Genome Biol. *19*, 221.

Georgatos, S.D., Pyrpasopoulou, A., and Theodoropoulos, P.A. (1997). Nuclear envelope breakdown in mammalian cells involves stepwise lamina disassembly and microtubule-drive deformation of the nuclear membrane. J. Cell Sci. *110 (Pt 17)*, 2129–2140.

Gerace, L., and Blobel, G. (1980). The nuclear envelope lamina is reversibly depolymerized during mitosis. Cell *19*, 277–287.

Gerace, L., Blum, A., and Blobel, G. (1978). Immunocytochemical localization of the major polypeptides of the nuclear pore complex-lamina fraction. Interphase and mitotic distribution. J. Cell Biol. *79*, 546–566.

Gerhard-Herman, M., Smoot, L.B., Wake, N., Kieran, M.W., Kleinman, M.E., Miller, D.T., Schwartzman, A., Giobbie-Hurder, A., Neuberg, D., and Gordon, L.B. (2012). Mechanisms of premature vascular aging in children with Hutchinson-Gilford progeria syndrome. Hypertension *59*, 92–97.

Gesson, K., Rescheneder, P., Skoruppa, M.P., von Haeseler, A., Dechat, T., and Foisner, R. (2016). A-type lamins bind both hetero- and euchromatin, the latter being regulated by lamina-associated polypeptide 2 alpha. Genome Res. *26*, 462–473.

Goldman, A.E., Maul, G., Steinert, P.M., Yang, H.Y., and Goldman, R.D. (1986). Keratin-like proteins that coisolate with intermediate filaments of BHK-21 cells are nuclear lamins. Proc. Natl. Acad. Sci. U. S. A. *83*, 3839–3843.

Goldman, A.E., Moir, R.D., Montag-Lowy, M., Stewart, M., and Goldman, R.D. (1992). Pathway of incorporation of microinjected lamin A into the nuclear envelope. J. Cell Biol. *119*, 725–735.

Goldman, R.D., Shumaker, D.K., Erdos, M.R., Eriksson, M., Goldman, A.E., Gordon, L.B., Gruenbaum, Y., Khuon, S., Mendez, M., Varga, R., et al. (2004). Accumulation of mutant lamin A causes progressive changes in nuclear architecture in Hutchinson-Gilford progeria syndrome. Proc. Natl. Acad. Sci. U. S. A. *101*, 8963–8968.

Gordon, C.M., Gordon, L.B., Snyder, B.D., Nazarian, A., Quinn, N., Huh, S., Giobbie-Hurder, A., Neuberg, D., Cleveland, R., Kleinman, M., et al. (2011). Hutchinson-Gilford progeria is a skeletal dysplasia. J. Bone Miner. Res. *26*, 1670–1679.

Gordon, L.B., Brown, W.T., and Collins, F.S. (2003). Hutchinson-Gilford Progeria Syndrome. In GeneReviews®, M.P. Adam, H.H. Ardinger, R.A. Pagon, S.E. Wallace, L.J.H. Bean, K. Stephens, and A. Amemiya, eds. (Seattle (WA): University of Washington, Seattle),.

Gordon, L.B., McCarten, K.M., Giobbie-Hurder, A., Machan, J.T., Campbell, S.E., Berns, S.D., and Kieran, M.W. (2007). Disease progression in Hutchinson-Gilford progeria syndrome: impact on growth and development. Pediatrics *120*, 824–833.

Gordon, L.B., Rothman, F.G., López-Otín, C., and Misteli, T. (2014). Progeria: a paradigm for translational medicine. Cell *156*, 400–407.

Guelen, L., Pagie, L., Brasset, E., Meuleman, W., Faza, M.B., Talhout, W., Eussen, B.H., de Klein, A., Wessels, L., de Laat, W., et al. (2008). Domain organization of human chromosomes revealed by mapping of nuclear lamina interactions. Nature *453*, 948–951.

Gupta, S., Stamatoyannopoulos, J.A., Bailey, T.L., and Noble, W.S. (2007). Quantifying similarity between motifs. Genome Biol. *8*, R24.

Heald, R., and McKeon, F. (1990). Mutations of phosphorylation sites in lamin A that prevent nuclear lamina disassembly in mitosis. Cell *61*, 579–589.

Hozák, P., Sasseville, A.M., Raymond, Y., and Cook, P.R. (1995). Lamin proteins form an internal

nucleoskeleton as well as a peripheral lamina in human cells. J. Cell Sci. *108 (Pt 2)*, 635–644.

Ikegami, K., Egelhofer, T.A., Strome, S., and Lieb, J.D. (2010). Caenorhabditis elegans chromosome arms are anchored to the nuclear membrane via discontinuous association with LEM-2. Genome Biol. *11*, R120.

Jiang, X.R., Jimenez, G., Chang, E., Frolkis, M., Kusler, B., Sage, M., Beeche, M., Bodnar, A.G., Wahl, G.M., Tlsty, T.D., et al. (1999). Telomerase expression in human somatic cells does not induce changes associated with a transformed phenotype. Nat. Genet. *21*, 111–114.

Johnson, W.E., Li, C., and Rabinovic, A. (2007). Adjusting batch effects in microarray expression data using empirical Bayes methods. Biostatistics *8*, 118–127.

Kim, D., Pertea, G., Trapnell, C., Pimentel, H., Kelley, R., and Salzberg, S.L. (2013). TopHat2: accurate alignment of transcriptomes in the presence of insertions, deletions and gene fusions. Genome Biol. *14*, R36.

Kim, Y., Sharov, A.A., McDole, K., Cheng, M., Hao, H., Fan, C.-M., Gaiano, N., Ko, M.S.H., and Zheng, Y. (2011). Mouse B-type lamins are required for proper organogenesis but not by embryonic stem cells. Science *334*, 1706–1710.

Kochin, V., Shimi, T., Torvaldson, E., Adam, S.A., Goldman, A., Pack, C.-G., Melo-Cardenas, J., Imanishi, S.Y., Goldman, R.D., and Eriksson, J.E. (2014). Interphase phosphorylation of lamin A. J. Cell Sci. *127*, 2683–2696.

Kulakovskiy, I.V., Vorontsov, I.E., Yevshin, I.S., Sharipov, R.N., Fedorova, A.D., Rumynskiy, E.I., Medvedeva, Y.A., Magana-Mora, A., Bajic, V.B., Papatsenko, D.A., et al. (2018). HOCOMOCO: towards a complete collection of transcription factor binding models for human and mouse via large-scale ChIP-Seq analysis. Nucleic Acids Res. *46*, D252–D259.

Lee, D.C., Welton, K.L., Smith, E.D., and Kennedy, B.K. (2009). A-type nuclear lamins act as transcriptional repressors when targeted to promoters. Exp. Cell Res. *315*, 996–1007.

Lee, S.-J., Jung, Y.-S., Yoon, M.-H., Kang, S.-M., Oh, A.-Y., Lee, J.-H., Jun, S.-Y., Woo, T.-G., Chun, H.-Y., Kim, S.K., et al. (2016). Interruption of progerin-lamin A/C binding ameliorates Hutchinson-Gilford progeria syndrome phenotype. J. Clin. Invest. *126*, 3879–3893.

Leemans, C., van der Zwalm, M.C.H., Brueckner, L., Comoglio, F., van Schaik, T., Pagie, L., van Arensbergen, J., and van Steensel, B. (2019). Promoter-Intrinsic and Local Chromatin Features Determine Gene Repression in LADs. Cell *177*, 852–864.e14.

Love, M.I., Huber, W., and Anders, S. (2014). Moderated estimation of fold change and dispersion for RNA-seq data with DESeq2. Genome Biol. *15*, 550.

Lund, E., Oldenburg, A.R., and Collas, P. (2014). Enriched domain detector: a program for detection of wide genomic enrichment domains robust against local variations. Nucleic Acids Res. *42*, e92.

Machanick, P., and Bailey, T.L. (2011). MEME-ChIP: motif analysis of large DNA datasets. Bioinformatics *27*, 1696–1697.

McCord, R.P., Nazario-Toole, A., Zhang, H., Chines, P.S., Zhan, Y., Erdos, M.R., Collins, F.S., Dekker, J., and Cao, K. (2012). Correlated alterations in genome organization, histone methylation, and DNA-lamin A/C interactions in Hutchinson-Gilford progeria syndrome. Genome Res. *23*, 260–269.

Merideth, M.A., Gordon, L.B., Clauss, S., Sachdev, V., Smith, A.C.M., Perry, M.B., Brewer, C.C., Zalewski, C., Kim, H.J., Solomon, B., et al. (2008). Phenotype and course of Hutchinson-Gilford progeria syndrome. N. Engl. J. Med. *358*, 592–604.

Meuleman, W., Peric-Hupkes, D., Kind, J., Beaudry, J.-B., Pagie, L., Kellis, M., Reinders, M., Wessels, L., and van Steensel, B. (2012). Constitutive nuclear lamina-genome interactions are highly conserved and associated with A/T-rich sequence. Genome Res. *23*, 270–280.

Moir, R.D., Montag-Lowy, M., and Goldman, R.D. (1994). Dynamic properties of nuclear lamins: lamin B is associated with sites of DNA replication. J. Cell Biol. *125*, 1201–1212.

Naetar, N., Korbei, B., Kozlov, S., Kerenyi, M.A., Dorner, D., Kral, R., Gotic, I., Fuchs, P., Cohen, T.V., Bittner, R., et al. (2008). Loss of nucleoplasmic LAP2alpha-lamin A complexes causes erythroid and epidermal progenitor hyperproliferation. Nat. Cell Biol. *10*, 1341–1348.

Olive, M., Harten, I., Mitchell, R., Beers, J.K., Djabali, K., Cao, K., Erdos, M.R., Blair, C., Funke, B., Smoot, L., et al. (2010). Cardiovascular pathology in Hutchinson-Gilford progeria: correlation with the vascular pathology of aging. Arterioscler. Thromb. Vasc. Biol. *30*, 2301–2309.

Peter, M., Nakagawa, J., Dorée, M., Labbé, J.C., and Nigg, E.A. (1990). In vitro disassembly of the nuclear lamina and M phase-specific phosphorylation of lamins by cdc2 kinase. Cell *61*, 591–602.

Picelli, S., Björklund, A.K., Reinius, B., Sagasser, S., Winberg, G., and Sandberg, R. (2014). Tn5 transposase and tagmentation procedures for massively scaled sequencing projects. Genome Res. *24*, 2033–2040.

Pickersgill, H., Kalverda, B., de Wit, E., Talhout, W., Fornerod, M., and van Steensel, B. (2006). Characterization of the Drosophila melanogaster genome at the nuclear lamina. Nat. Genet. *38*, 1005–1014.

Piñero, J., Bravo, À., Queralt-Rosinach, N., Gutiérrez-Sacristán, A., Deu-Pons, J., Centeno, E., García-García, J., Sanz, F., and Furlong, L.I. (2017). DisGeNET: a comprehensive platform integrating information on human disease-associated genes and variants. Nucleic Acids Res. *45*, D833–D839.

Prakash, A., Gordon, L.B., Kleinman, M.E., Gurary, E.B., Massaro, J., D'Agostino, R., Sr, Kieran, M.W., Gerhard-Herman, M., and Smoot, L. (2018). Cardiac Abnormalities in Patients With Hutchinson-Gilford Progeria Syndrome. JAMA Cardiol *3*, 326–334.

Quinlan, A.R., and Hall, I.M. (2010). BEDTools: a flexible suite of utilities for comparing genomic features. Bioinformatics *26*, 841–842.

Reddy, K.L., Zullo, J.M., Bertolino, E., and Singh, H. (2008). Transcriptional repression mediated by repositioning of genes to the nuclear lamina. Nature *452*, 243–247.

Reznikoff, W.S. (2008). Transposon Tn5. Annu. Rev. Genet. *42*, 269–286.

Roadmap Epigenomics Consortium, Kundaje, A., Meuleman, W., Ernst, J., Bilenky, M., Yen, A., Heravi-Moussavi, A., Kheradpour, P., Zhang, Z., Wang, J., et al. (2015). Integrative analysis of 111 reference human epigenomes. Nature *518*, 317–330.

Sanjana, N.E., Shalem, O., and Zhang, F. (2014). Improved vectors and genome-wide libraries for CRISPR screening. Nat. Methods *11*, 783–784.

Shimi, T., Pfleghaar, K., Kojima, S.-I., Pack, C.-G., Solovei, I., Goldman, A.E., Adam, S.A., Shumaker, D.K., Kinjo, M., Cremer, T., et al. (2008). The A- and B-type nuclear lamin networks: microdomains involved in chromatin organization and transcription. Genes Dev. *22*, 3409–3421.

Shumaker, D.K., Dechat, T., Kohlmaier, A., Adam, S.A., Bozovsky, M.R., Erdos, M.R., Eriksson, M., Goldman, A.E., Khuon, S., Collins, F.S., et al. (2006). Mutant nuclear lamin A leads to progressive alterations of epigenetic control in premature aging. Proc. Natl. Acad. Sci. U. S. A. *103*, 8703–8708.

Sieprath, T., Corne, T.D.J., Nooteboom, M., Grootaert, C., Rajkovic, A., Buysschaert, B., Robijns, J., Broers, J.L.V., Ramaekers, F.C.S., Koopman, W.J.H., et al. (2015). Sustained accumulation of prelamin A and depletion of lamin A/C both cause oxidative stress and mitochondrial dysfunction but induce different cell fates. Nucleus *6*, 236–246.

Silvera, V.M., Gordon, L.B., Orbach, D.B., Campbell, S.E., Machan, J.T., and Ullrich, N.J. (2013). Imaging characteristics of cerebrovascular arteriopathy and stroke in Hutchinson-Gilford progeria syndrome. AJNR Am. J. Neuroradiol. *34*, 1091–1097.

Simon, D.N., and Wilson, K.L. (2013). Partners and post-translational modifications of nuclear lamins. Chromosoma *122*, 13–31.

van Steensel, B., and Belmont, A.S. (2017). Lamina-Associated Domains: Links with Chromosome Architecture, Heterochromatin, and Gene Repression. Cell *169*, 780–791.

Stewart, S.A., Dykxhoorn, D.M., Palliser, D., Mizuno, H., Yu, E.Y., An, D.S., Sabatini, D.M., Chen, I.S.Y., Hahn, W.C., Sharp, P.A., et al. (2003). Lentivirus-delivered stable gene silencing by RNAi in primary cells. RNA *9*, 493–501.

Stierlé, V., Couprie, J., Ostlund, C., Krimm, I., Zinn-Justin, S., Hossenlopp, P., Worman, H.J., Courvalin, J.-C., and Duband-Goulet, I. (2003). The carboxyl-terminal region common to lamins A and C contains a DNA binding domain. Biochemistry *42*, 4819–4828.

Swift, J., Ivanovska, I.L., Buxboim, A., Harada, T., Dingal, P.C.D.P., Pinter, J., Pajerowski, J.D., Spinler, K.R., Shin, J.-W., Tewari, M., et al. (2013). Nuclear lamin-A scales with tissue stiffness and enhances matrix-directed differentiation. Science *341*, 1240104–1240104.

Tanaka, E., Bailey, T., Grant, C.E., Noble, W.S., and Keich, U. (2011). Improved similarity scores for comparing motifs. Bioinformatics *27*, 1603–1609.

Taniura, H., Glass, C., and Gerace, L. (1995). A chromatin binding site in the tail domain of nuclear lamins that interacts with core histones. J. Cell Biol. *131*, 33–44.

Torvaldson, E., Kochin, V., and Eriksson, J.E. (2015). Phosphorylation of lamins determine their structural properties and signaling functions. Nucleus *6*, 166–171.

Tripathi, S., Pohl, M.O., Zhou, Y., Rodriguez-Frandsen, A., Wang, G., Stein, D.A., Moulton, H.M., DeJesus, P., Che, J., Mulder, L.C.F., et al. (2015). Meta- and Orthogonal Integration of Influenza "OMICs" Data Defines a Role for UBR4 in Virus Budding. Cell Host Microbe *18*, 723–735.

Ward, G.E., and Kirschner, M.W. (1990). Identification of cell cycle-regulated phosphorylation sites on nuclear lamin C. Cell *61*, 561–577.

Worman, H.J., Fong, L.G., Muchir, A., and Young, S.G. (2009). Laminopathies and the long strange trip from basic cell biology to therapy. J. Clin. Invest. *119*, 1825–1836.

Xie, C., and Tammi, M.T. (2009). CNV-seq, a new method to detect copy number variation using high-throughput sequencing. BMC Bioinformatics *10*, 80.

Zhang, J., Lian, Q., Zhu, G., Zhou, F., Sui, L., Tan, C., Mutalif, R.A., Navasankari, R., Zhang, Y., Tse, H.-F., et al. (2011). A human iPSC model of Hutchinson Gilford Progeria reveals vascular smooth muscle and mesenchymal stem cell defects. Cell Stem Cell *8*, 31–45.

Zhang, Y., Liu, T., Meyer, C.A., Eeckhoute, J., Johnson, D.S., Bernstein, B.E., Nusbaum, C., Myers, R.M., Brown, M., Li, W., et al. (2008). Model-based analysis of ChIP-Seq (MACS). Genome Biol. *9*, R137.

Zheng, X., Hu, J., Yue, S., Kristiani, L., Kim, M., Sauria, M., Taylor, J., Kim, Y., and Zheng, Y. (2018). Lamins Organize the Global Three-Dimensional Genome from the Nuclear Periphery. Mol. Cell *71*, 802–815.e7.

Zhou, Y., Zhou, B., Pache, L., Chang, M., Khodabakhshi, A.H., Tanaseichuk, O., Benner, C., and Chanda, S.K. (2019). Metascape provides a biologist-oriented resource for the analysis of systems-level datasets. Nat. Commun. *10*, 1523.